The Canadian Journal of Mineralogy and Petrology
ISSN 2817-1713
Vol. 63, pp. 809-831 (2025)
DOI: 10.3749/2500001

MINERALOGY AND GEOCHEMISTRY OF ALUMINUM PHOSPHATES FROM THE MONTEBRAS PEGMATITE, MASSIF CENTRAL, FRANCE

Cassian PIRARD, Martin DEPRET, and Frederic HATERT[§]

Laboratoire de Minéralogie, Département de Géologie, Université de Liège, Bâtiment B18, Sart Tilman,
B-4000 Liège, Belgium

Abstract

The Montebras pegmatitic cupola, Massif Central, France, hosts large pods of aluminum phosphates mainly composed of primary amblygonite–montebrasite. These phosphate masses are considerably altered by post-magmatic processes, leading to the formation of a number of secondary metasomatic hydrothermal phosphates (lacroixite, wardite, morinite, viitaniemiite, fluorapatite, triplite, eosphorite) and low-temperature phosphates (fluorapatite, crandallite, goyazite, gorceixite, variscite, turquoise, wavellite). A Mn-rich viitaniemiite-like phase, as well as an unknown Na-Al-P fluoride, were also identified. These phosphate assemblages were first observed with a classical polarizing microscope, but we demonstrated that cathodoluminescence microscopy was a powerful tool to decipher the complex petrography of these phases. Electron-microprobe analyses, as well as laser ablation inductively coupled plasma-mass spectroscopy, were used to characterize the trace- and major-elemental composition of those phosphates. These results allowed the determination of genetic sequences, explaining the crystallization of aluminum phosphates at different stages of the Montebras pegmatite evolution.

Keywords: aluminum phosphates, granitic pegmatite, amblygonite–montebrasite, lacroixite, Montebras, France, cathodoluminescence, trace elements.

Introduction

Phosphate minerals are important accessory phases in rare-element granitic pegmatites belonging to the LCT (Lithium-Cesium-Tantalum) petrogenetic family, with aluminum phosphates of the amblygonite–montebrasite series generally occurring in pegmatites of the amblygonite subtype (Černý & Ercit 2005). When compared to silicates, phosphate minerals present narrower stability fields and are therefore very sensitive to the variations of physicochemical parameters. This feature implies the formation of a high number of secondary phosphates during subsolidus hydrothermal and meteoric processes (Mason 1941, Moore 1982, Fransolet *et al.* 2007, Galliski *et al.* 2012, Baijot *et al.* 2012, Vignola 2018, Vignola *et al*. 2011). Petrographical, mineralogical, and geochemical investigations of phosphate minerals are consequently of prime interest for the understanding of granitic pegmatite evolution processes (Prado Araujo *et al.* 2023a).

Alfred Lacroix described the mineralogy of the Montebras pegmatite body, Massif Central, France, more than a century ago (Lacroix 1910), preceded by the discovery of new phosphate species morinite (Lacroix 1891) and montebrasite (Moissenet 1871). Some general studies were also performed in the past, mainly concerning the geology of the Montebras granitic cupola (Aubert 1969, Marcoux *et al.* 2021), or giving detailed systematic mineralogy descriptions (Patureau *et al.* 2011). However, to date, a comprehensive investigation of the phosphate mineral associations of Montebras, and of their petrogenetic significance, has never been realized.

In this paper, we investigated several aluminum phosphate samples from the Montebras pegmatite, collected in the field or occurring in the collections of the Liège University and of the School of Mines in Paris ("Ecole Nationale Supérieure des Mines de Paris", ENSMP). Thin sections cut from these samples were observed under the polarizing microscope for their petrographic characterization, and the mineral phases were analyzed by electron microprobe and laser ablation inductively coupled plasma-mass spectroscopy (LA-ICP-MS) methods. The identification of accessory mineral phases was

---

[§] *Corresponding author e-mail address*: fhatert@uliege.be

TABLE 1. LIST OF SAMPLES FROM MONTEBRAS INVESTIGATED IN THIS STUDY

Sample #	Uliège #	ENSMP #	Comments	Old numbers
MONT1	179	–	–	–
MONT1	43	–	–	–
MONT2	A607	–	–	–
MONT3	Montebras	–	Collected by Bourguignon	–
MONT4	–	28889	Bernard, 27-M1766	27-M1766
MONT5	–	38507	Collected by Mallard, 1885	–
MONT6	–	32465	Mine Le Communal	–
MONT7	–	17352	SCEM, 1965	–
MONT8	–	39950	–	–
MONT9	–	4837	Collected by Lacroix, 1890	3-M5847
MONT10	–	28732	Bertrand Emile collection	1871 (Adam 4485)
MONT11	–	52512	–	–
MONT12	–	5838	Collected by Morineau, 1891	M6192
MONT13	–	51297	–	–
MONT14	–	7836	–	19.5241
MONT15	Montebras	–	–	–

confirmed by X-ray powder diffraction measurements, and cathodoluminescence microscopic observations were conducted to more accurately decipher the petrographic relationships among phosphates. The present paper gives the results of these investigations and provides new insights on the transformation sequences, crystal chemistry, and trace element behavior in these minerals.

Geological Context

The Montebras pegmatite is a famous deposit in the Massif Central, France, and the type locality for the two species morinite (Lacroix 1891) and montebrasite (Moissenet 1871). It lies on the northwestern margin of the Hercynian belt and is located in a magmatic complex formed by an albitic leucogranite and a microgranite intruded in the peraluminous Chanon granitic batholith (Aubert 1969). The Montebras albitic leucogranite (~310 ± 5 Ma, Melleton *et al.* 2015, Marcoux *et al.* 2021), emplaced between the microgranite and the Chanon batholith, forms in its uppermost part a cupola reaching several meters in thickness and containing a pegmatite body, a quartz-rich layer, and a mica-rich greisen (Aubert 1969, Dudoignon *et al.* 1988, Charoy & Noronha 1999).

The pegmatite is mainly composed of K-feldspar, quartz, albite, Li-bearing micas, apatite-group minerals, topaz, some centimeter-sized amblygonite–montebrasite, as well as minor turquoise pods, kaolinite, cassiterite, W, Cu, and As mineralizations. The transition to the quartz-rich layer shows a decrease in the feldspar content and is characterized by large aggregates of cassiterite, muscovite, blue fluorapatite, and large blocks of Al-rich phosphates (Moissenet 1871, Aubert 1969, Marcoux *et al.* 2021).

The pegmatite body has been successively mined for variscite and/or turquoise in prehistoric times (Balagny 1939), for tin in the 19th century (Mallard 1859), and for amblygonite and feldspar in the first part of the 20th century (Aubert 1969). Recently, new mining activities for feldspar have led to a new characterization of the ore body (Marcoux *et al.* 2021).

Samples used in this study mostly come from the quartz-rich facies and are part of the collections of the Laboratory of Mineralogy of the Liège University (ULiège) and the School of Mines of Paris (ENSMP). Several samples were collected by Alfred Lacroix in the original mineralogical study of the deposit (Lacroix 1891, 1910) (Table 1).

Analytical Methods

Samples were first observed with a stereomicroscope and in thin section under a polarizing microscope (Leica DMLP) at the Laboratory of Mineralogy of the Liège University. However, some difficulties in observing the petrological relationships or some textures in aluminum phosphates led us to perform many microscopic observations with a cathodoluminescence (CL) microscope. This instrument was an Olympus BX50 microscope equipped with a CITL cold cathode luminescence 8200 mk3, housed in the EDDyLab (ULiège). Observations were made at 0.05 mbar with an electronic voltage of 15 ± 2 kV and a current of 700±50 μA. Cathodoluminescence spectra were obtained with a hot cathode system on a JEOL JXA8200 at the Advanced Analytical Centre (James Cook University, Australia), and then processed with the XCLent software.

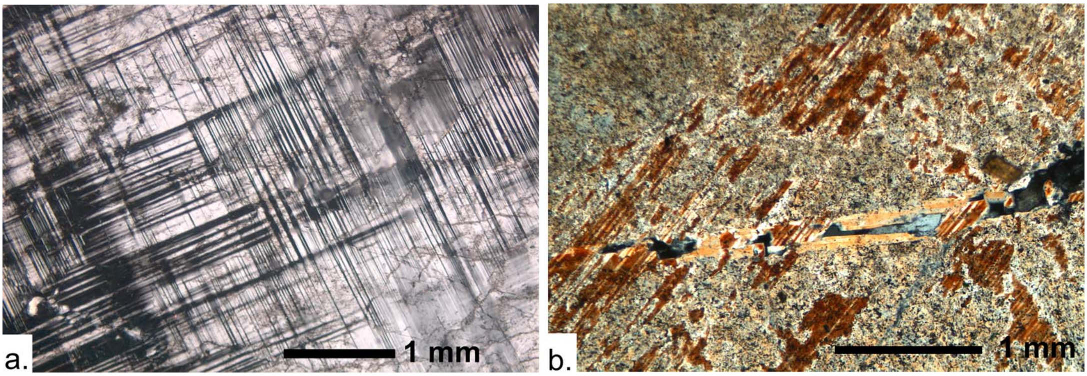

FIG. 1. (A) Primary amblygonite showing characteristic twinning in crossed-polarized light (sample MONT3). (B) Primary (gray), secondary (orange-brown), and ternary (yellow) amblygonite–montebrasite in crossed-polarized light (sample MONT9).

Less common minerals were identified by X-ray powder diffraction measurements (XRPD) on a Philips PW-3710 diffractometer equipped with a graphite monochromator and using Cu$K\alpha$ ($\lambda = 1.5418$ Å) or Fe$K\alpha$ ($\lambda = 1.9373$ Å) radiation sources (Laboratory of Mineralogy, ULiège). For microscopic grains, XRPD measurements were performed with a Debye-Scherrer camera (diameter = 114.6 mm) mounted on the same X-ray sources. Unit-cell parameters were calculated through the least-square refinement program LCLSQ v.8.4 (Burnham 1991) using *d* values corrected with an internal $Pb(NO_3)_2$ standard.

Chemical analyses were performed with a CAMECA SX-50 electron microprobe (Ruhr-Universität Bochum, Germany) using an accelerating voltage of 15 kV, a beam current of 8 nA, and a beam diameter of 10 μm. Standards used were jadeite (Na), synthetic glasses (K, Ba), spessartine (Al, Mn), andradite (Si, Fe, Ca), graftonite (P), $SrCu_4Si_4O_{10}$ (Sr, Cu), pyrope (Mg), and topaz (F). The counting time per element is 30 s, or 15 s for the most beam-sensitive phases. Fluorine was measured with a 120 s counting time, on a PC0 crystal. Beam-sensitive phase analyses were doubled checked with a JEOL 6400 scanning electron microscope (15 kV, 1 nA, 1 μm beam diameter) at the Electron Microscopy Unit of the Australian National University (ANU), using an energy dispersive spectrometer (EDS) calibrated on known mineral standards (120 s counting time). Fluorine in lacroixite, fluorapatite, morinite, and "F-phase" has been analyzed on a JEOL JXA8200 instrument located at the Advanced Analytical Centre (JCU), using 15 kV acceleration voltage and 14.5 nA beam current. Fluorine was measured using a time-zero integrated analysis where F$K\alpha$ is monitored for 35 s on a TAP crystal and then regressed to provide the initial value.

Infrared spectra were obtained on a Nicolet Nexus FTIR spectrometer located at the Laboratory of Mineralogy (ULiège). Spectra were measured between 400 and 4000 cm^{-1} and reconstructed by the addition of 32 scans with a 1 cm^{-1} resolution. The infrared source is heated SiC (Ever-Glo). Samples were prepared through a mixture with KBr (1:74), producing a 150 mg pressed pellet dried at 110 °C and analyzed in a dry atmosphere.

Trace element analyses were obtained using laser ablation inductively coupled plasma-mass spectrometry (LA-ICP-MS) at the Research School of Earth Science (RSES, ANU) using a pulsed 193 mm ArF Excimer laser with 3–7 mJ of output energy, reaching the sample at a repetition rate of 5 Hz (Eggins *et al.* 1998) and coupled to an Agilent HP7500 quadrupole ICP-MS system. Laser sampling was performed in an Ar atmosphere with He: H_2 (ratio 15:1) as a carrier gas, and with a beam size of 30–50 μm in diameter. ^{27}Al was the internal standard and NIST SRM 612 glass the external standard, with reference data from Spandler *et al.* (2011). BCR-2G glass was used as a secondary standard and reproducibility was better than ±7%.

CHARACTERIZATION OF PHOSPHATE MINERALS

Li-bearing phosphates

Minerals of the amblygonite–montebrasite series, $LiAl(PO_4)(F,OH)$, constitute the main primary phase in the phosphate assemblages of Montebras. They occur as centimeter-sized (or larger) masses showing colorless to white colors, sometimes greenish blue, or with lilac hues. These phosphates frequently form idiomorphic crystals often altered by quartz, lacroixite, fluorapatite, and hydrous phosphates. Fresh amblygonite–montebrasite looks light gray, while more altered zones are whiter and seem less transparent. In thin sections, primary amblygonite (Fig. 1a) is often replaced by secondary montebrasite (rarely amblygonite) along cleavage and twinning planes and cracks. In some samples, late generation of tertiary

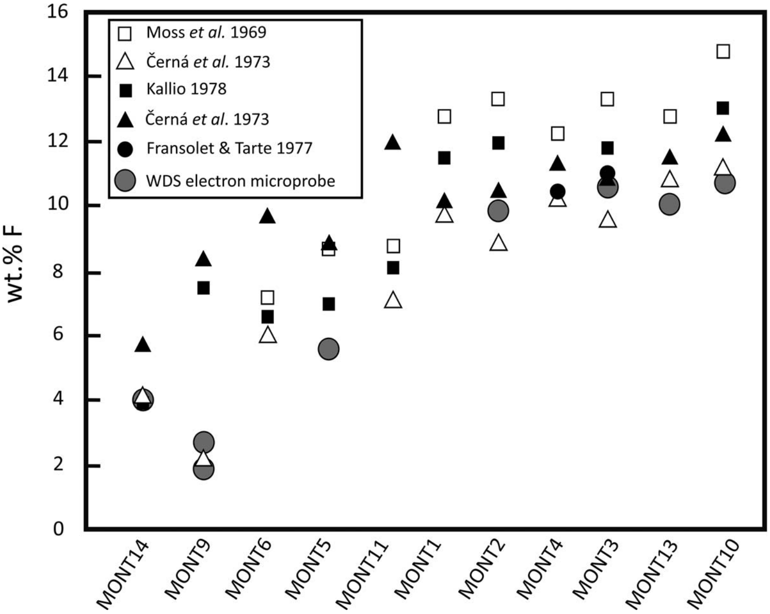

FIG. 2. Comparison of fluorine content estimation in amblygonite–montebrasite, based on X-ray diffraction (Moss *et al*. 1969, Černá *et al.* 1973, Kallio 1978), infrared spectroscopy (Fransolet & Tarte 1977), and electron probe microanalysis (WDS). Double data points for WDS analyses are produced by primary and secondary amblygonite–montebrasite in single samples.

montebrasite is observed in quartz veins cross-cutting both amblygonite–montebrasite generations (Fig. 1b).

Electron probe microanalyses (EPMA) show that primary montebrasites present the highest fluorine contents (>10 wt.% F), while secondary montebrasite range from 6 to 3 wt.% F (Fig. 2 and Table 2). Veinlets of tertiary montebrasite crossing through first and second generation of amblygonite–montebrasite are hydroxyl-rich (below 1 wt.% F; Table 2). Na_2O content in all amblygonite–montebrasite is below 0.1 wt.%, and higher values are clearly correlated with lacroixite contamination, as observed in CL imaging (see below). Cathodoluminescence for amblygonite–montebrasite is weak with little variation between the different generations. However, we clearly observed color variations between samples, ranging from blue luminescence (489 to 498 nm) to red luminescence (655 nm) (Fig. $3a_3$, $3b_3$).

Trace element contents in primary and secondary amblygonite–montebrasite have similar ranges and only display rare differences (Fig. 4). Although Al^{3+} in montebrasite is known to allow substitution with trivalent and tetravalent cations (Dias *et al*. 2011), most anomalies and variability between trace elements concentrations seem to be linked to the presence of micro-inclusions, as is known in such phosphates (Shirose & Uehara 2014). Veinlets of tertiary montebrasite, which are more transparent, have smoother trace element patterns and display a clear enrichment in medium rare earth elements (REE) over light and heavy REE, as well as an enrichment in alkali and transition metals.

Na-bearing phosphates

Lacroixite, $NaAlPO_4F$, is present in all samples as a diffuse alteration of amblygonite–montebrasite, occurring as a micron-size mesh, and occasionally showing submillimeter whitish veinlets (Fig. 5a). Optical microscopy observations remain difficult due to the submicroscopic meshy texture and similar optical properties with amblygonite that lead to the erroneous identification of "natromontrebasite" in many pegmatites (Fransolet *et al.* 2007). In the studied samples, cathodoluminescence is a very powerful tool to identify lacroixite in amblygonite (Figs. $3b_3$, 5b, 6a). Early lacroixite has a yellow-green luminescence (549 nm), while later lacroixite has a blue-greenish luminescence (487 to 513 nm), contrasting with the duller background colors of amblygonite–montebrasite. Occasionally, secondary euhedral lacroixite grows on vein walls (Fig. 5a), reaching up to ~100 µm in length and often associated with fluorapatite and "F-phase"s.

X-ray diffraction and EPMA of lacroixite provide chemical data near the ideal composition, with a weak positive correlation between Na/(Na+Li) and F/(F+OH) (Table 3). Trace elements in meshy lacroixite show a non-systematic enrichment in U, Sr, Ba, Cs, Cu, and Cr, while lacroixite veins mostly show an enrichment in Cu,

TABLE 2. ELECTRON PROBE MICROANALYSES OF AMBLYGONITE-MONTEBRASITE FROM MONTEBRAS

Sample	MONT2	MONT2	MONT3	MONT5	MONT9	MONT9	MONT9	MONT10	MONT10	MONT10	MONT13	MONT14	MONT15	MONT15	ML19
Phase	I	II			I	II	III						I	II	
n	7	4	6	6	3	7	3	8	6	3	4	6	1	4	8
P_2O_5	49.22 (43)	49.83 (104)	49.95 (39)	50.79 (60)	50.17 (31)	49.44 (105)	50.79 (104)	50.04 (63)	49.59 (43)	50.18 (45)	50.20 (65)	50.22 (70)	49.97	49.92 (148)	46.02 (68)
Al_2O_3	34.42 (20)	34.45 (35)	34.67 (5)	34.89 (14)	34.32 (13)	34.78 (50)	34.51 (33)	34.86 (26)	34.44 (16)	35.13 (20)	34.75 (15)	35.27 (19)	34.74	34.97 (18)	31.64 (89)
Na_2O	0.80 (70)	1.44 (90)	tr.	bdl	bdl	bdl	bdl	0.11 (6)	0.13 (6)	0.11 (2)	bdl	tr.	bdl	bdl	bdl
F	9.90 (42)	6.59 (143)	10.64 (20)	5.64 (69)	3.63 (30)	1.77 (19)	0.78 (12)	10.69 (9)	9.52 (52)	5.88 (58)	10.03 (50)	4.00 (48)	10.42	4.60 (46)	3.29 (39)
Li_2O*	9.87 (39)	9.65 (57)	10.35 (7)	10.49 (11)	10.36 (3)	10.31 (17)	10.47 (15)	10.36 (8)	10.25 (8)	10.41 (8)	10.41 (8)	10.42 (12)	10.39	10.41 (20)	9.52 (19)
H_2O**	1.49 (20)	3.11 (75)	1.21 (7)	3.67 (34)	4.53 (13)	5.38 (13)	5.94 (9)	1.21 (7)	1.70 (24)	3.52 (27)	1.53 (21)	4.43 (23)	1.33	4.09 (26)	4.19 (26)
Total	105.70 (43)	105.06 (89)	106.89 (60)	105.53 (70)	103.04 (35)	101.71 (158)	102.49 (147)	107.27 (54)	105.62 (63)	105.23 (78)	106.95 (103)	104.47 (80)	106.84	104.00 (187)	94.69 (160)
Total-(O=F)	101.53 (41)	102.29 (116)	102.41 (53)	103.16 (62)	101.51 (27)	100.97 (157)	102.16 (144)	102.77 (55)	101.61 (49)	102.76 (68)	102.73 (88)	102.79 (74)	102.46	102.06 (188)	93.30 (168)
Cation numbers *pfu*															
P	1.01 (0)	1.01 (1)	1.01 (0)	1.02 (1)	1.02 (0)	1.01 (1)	1.02 (1)	1.01 (1)	1.01 (0)	1.01 (0)	1.01 (0)	1.01 (1)	1.01	1.01 (1)	1.02 (1)
Al	0.98 (1)	0.98 (1)	0.98 (0)	0.97 (1)	0.97 (1)	0.99 (1)	0.97 (1)	0.98 (1)	0.98 (1)	0.98 (1)	0.98 (1)	0.99 (1)	0.98	0.98 (2)	0.97 (1)
Na	0.04 (3)	0.07 (4)	tr.	bdl	bdl	bdl	bdl	0.01 (0)	0.01 (0)	0.01 (0)	bdl	tr.	bdl	bdl	bdl
F	0.76 (3)	0.50 (11)	0.81 (1)	0.42 (5)	0.27 (2)	0.14 (1)	0.06 (1)	0.81 (1)	0.73 (4)	0.44 (4)	0.76 (3)	0.30 (4)	0.79	0.35 (4)	0.27 (4)
Li*	0.96 (3)	0.93 (4)	1.00 (0)	1.00 (1)	1.00 (0)	1.00 (0)	1.00 (0)	0.99 (0)	0.99 (0)	0.99 (0)	1.00 (0)	0.99 (1)	1.00	1.00 (0)	1.00 (0)
OH**	0.24 (3)	0.50 (11)	0.19 (1)	0.58 (5)	0.73 (2)	0.86 (1)	0.94 (1)	0.19 (1)	0.27 (4)	0.56 (4)	0.24 (3)	0.70 (4)	0.21	0.65 (4)	0.73 (4)
Scat.	2.99 (0)	2.99 (0)	2.99 (0)	2.99 (0)	2.99 (0)	2.99 (1)	2.99 (0)	2.99 (0)	2.99 (0)	2.99 (0)	2.99 (0)	2.99 (0)	2.99	2.99 (1)	2.99 (1)
F/(F+OH)	0.76 (3)	0.50 (11)	0.81 (1)	0.42 (5)	0.27 (2)	0.14 (1)	0.06 (1)	0.81 (1)	0.73 (4)	0.44 (4)	0.76 (3)	0.30 (4)	0.79	0.35 (4)	0.27 (4)

Cation numbers were calculated on the basis of four anhydrous oxygens.

* Li calculated by difference to Na on the lithium site: Li = (1−Na).

** Hydroxyl groups calculated by difference on the fluorine site: OH = (1−F).

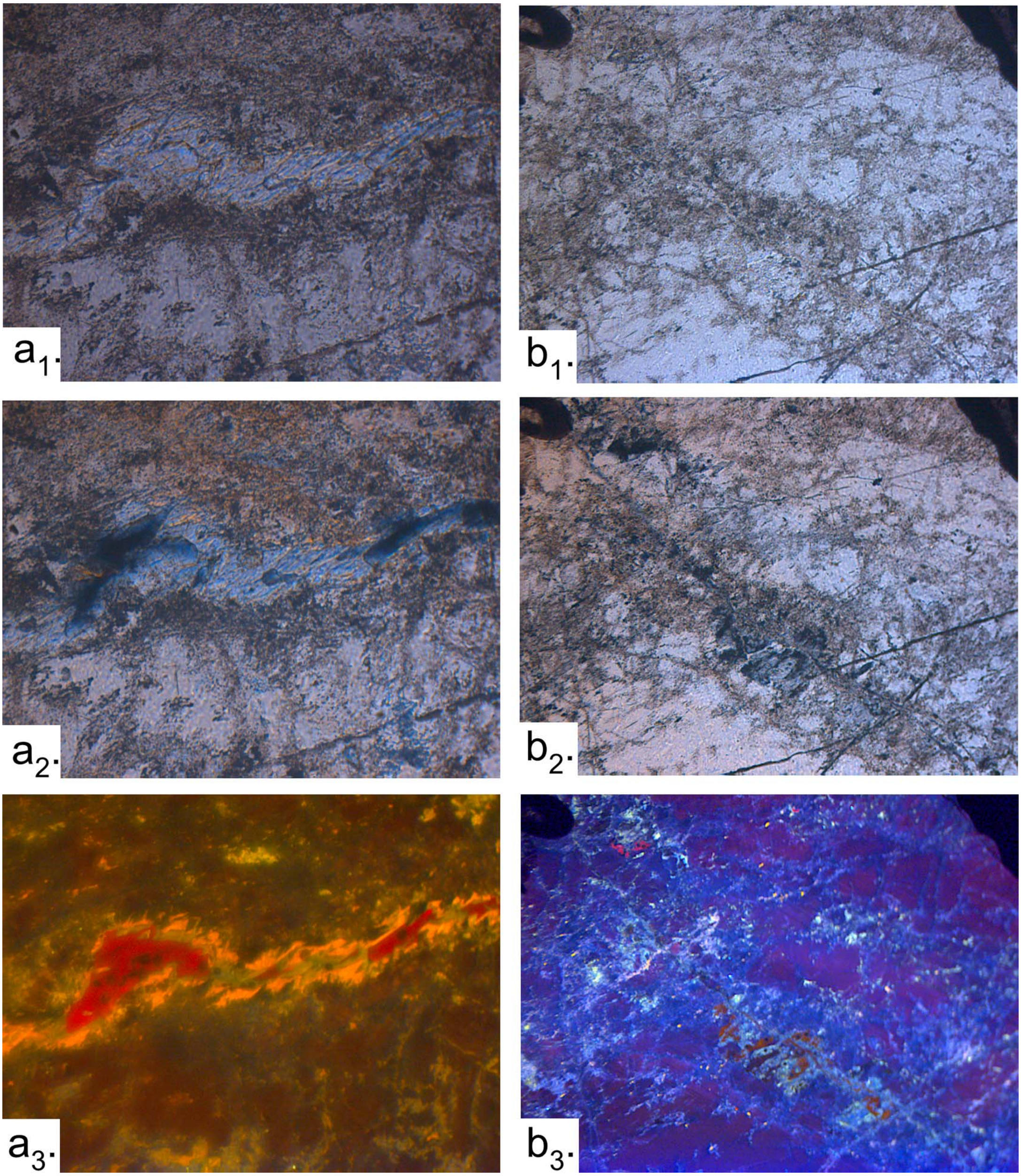

FIG. 3. Two assemblages of phosphate minerals observed under the microscope in plane-polarized light (a_1, b_1), crossed-polarized light (a_2, b_2), or cathodoluminescence (a_3, b_3). The mineral phases are only distinguishable in cathodoluminescence. a_3. Vein cross-cutting amblygonite (deep red) with two generations of lacroixite (yellow and blue-green) and "F-phase" (bright red) in cathodoluminescence (sample MONT2). b_3. Alteration-free amblygonite (purple) with lacroixite mesh replacement (blue) and viitaniemiite inclusions (red-orange) in cathodoluminescence (sample MONT12).

Cs, and U, as well as a slight depletion in other elements compared to the primary amblygonite (Fig. 4).

Wardite, $NaAl_3(PO_4)_2(OH)_4 \cdot 2H_2O$, has been observed and identified through X-ray powder diffraction and EPMA analyses. It occurs in alteration zones of quartz veins containing wavellite, variscite, turquoise, and fluorapatite. Important or complete replacement by fluorapatite is common (Fig. 6b). Chemical composition of wardite in

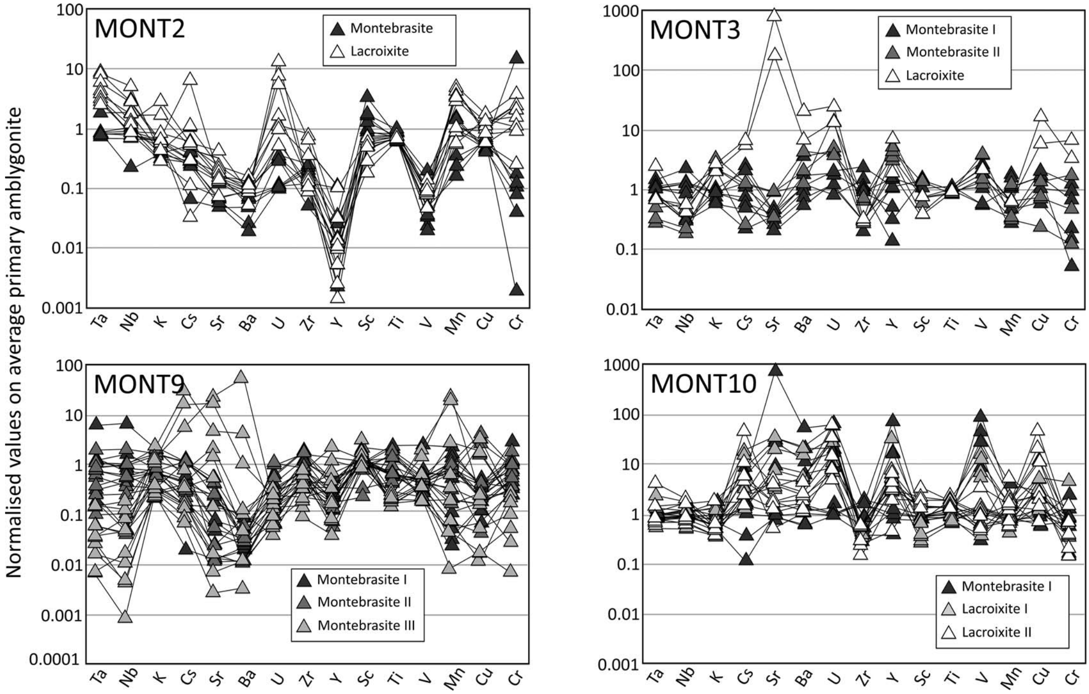

FIG. 4. Trace element contents in amblygonite–montebrasite and lacroixite. Values normalized on average primary MONT10 amblygonite values.

Montebras is $(Na_{0.94}Ca_{0.04}Mg_{0.01})Al_{2.95}(PO_4)_{2.05}(OH_{3.57}F_{0.37})\cdot 2H_2O$ (Table 4).

Na-Ca-bearing phosphates

Montebras is the type locality of morinite, $NaCa_2Al_2(PO_4)_2(F,OH)_5\cdot 2H_2O$ (Lacroix 1891), which occurs as purple-red masses and fibrous crusts with concentric color changes. Samples available for this study show morinite as a filling in late quartz veins with no amblygonite, in contrast with the original description of this mineral (Lacroix 1891, Lahti 1981). Minerals associated with morinite are crandallite, turquoise, and fluorapatite as a replacement (Fig. 6c). Cathodoluminescence is not

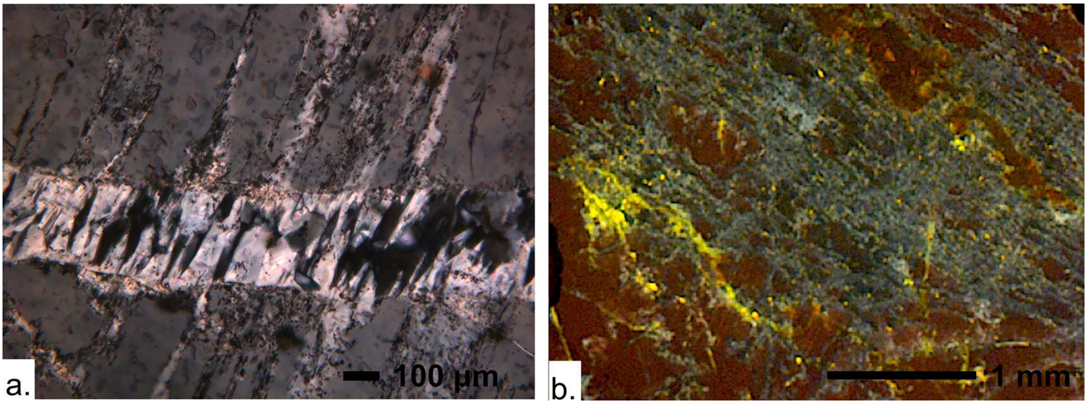

FIG. 5. (a) Sample showing submillimeter whitish veinlets of meshy lacroixite in amblygonite, as well as secondary euhedral lacroixite crystals growing on larger vein walls (sample MONT10, crossed-polarized light). (b) Early lacroixite disseminated in amblygonite and showing a yellow-green luminescence (549 nm) in CL microscopy (sample MONT2).

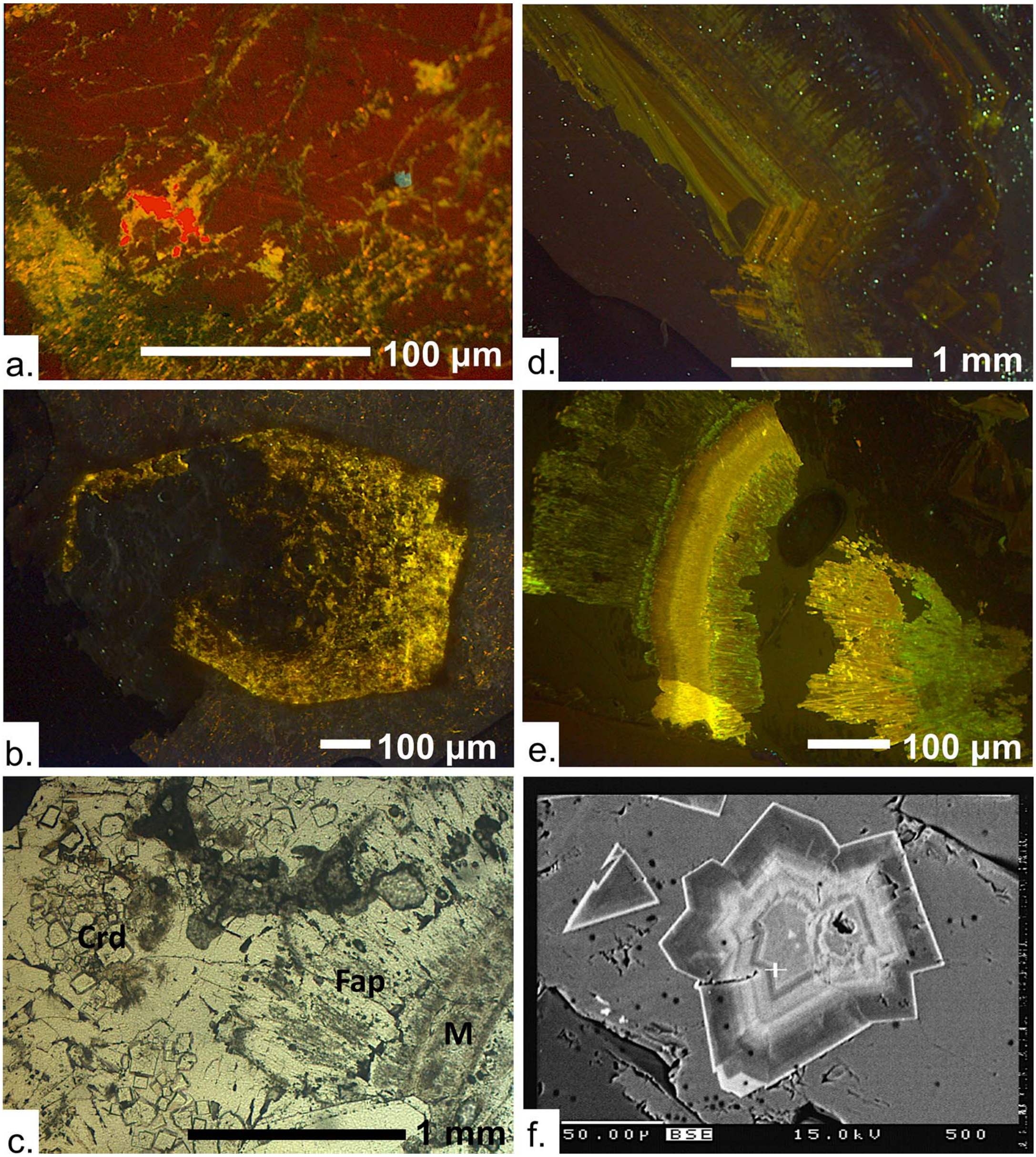

FIG. 6. (a) Vitaniemiite grain (orange-red) included in amblygonite showing brownish CL colors. Lacroixite-I (yellow-green) and lacroixite-II (blue-greenish) replace amblygonite (sample MONT2, CL microscopy). (b) Euhedral wardite crystal partially replaced by diffuse fluorapatite showing bright yellow CL colors (sample MONT3, CL microscopy). (c) Assemblage showing morinite (M) replaced by fibrous fluorapatite (Fap) and by crandallite euhedral crystals (Crd) (sample MONT12, plane-polarized light). (d) Growth zonation in morinite, with pink, orange, and brown CL colors (sample MONT12, CL microscopy). (e) Replacement of zoned morinite by fibrous Na-rich fluorapatite in cathodoluminescence (sample MONT12). (f) Euhedral crystal of crandallite showing a strong compositional zoning in back-scattered electron microscopy. Bright zones correspond to goyazite (Sr-rich), while dark zones correspond to crandallite (Ca-rich) (sample MONT12).

TABLE 3. ELECTRON PROBE MICROANALYSES OF LACROIXITE

Sample	MONT2-a	MONT2-b	MONT2-c	MONT2-d	MONT2-UCL	MONT2-UCL	MONT3-a	MONT10-a	MONT10-UCL	MONT13-a	MONT20-a
Phase	blue CL	yellow CL	cream CL	vein							
n	9	3	3	3	unk	unk	6	8	unk	2	5
P_2O_5	41.30 (14)	40.27 (63)	43.94 (23)	42.91 (148)	42.07 (195)	40.87 (159)	42.25 (179)	43.05 (80)	41.01 (104)	44.06 (93)	44.87 (69)
Al_2O_3	31.77 (11)	32.13 (17)	31.22 (33)	31.70 (56)	31.31 (21)	31.04 (45)	31.44 (26)	31.48 (64)	31.49 (14)	31.72 (95)	31.17 (34)
Na_2O	18.41 (22)	18.54 (5)	18.03 (14)	18.11 (19)	16.24 (136)	16.57 (206)	17.74 (74)	17.74 (74)	17.51 (51)	15.16 (75)	15.79 (86)
F	13.15 (263)	18.24 (74)	12.81 (47)	14.83 (215)	12.71 (257)	13.42 (292)	15.21 (108)	11.35 (43)	13.57 (37)	10.46 (31)	11.63 (53)
Li_2O*	tr.	bdl	0.46 (9)	0.36 (19)	1.05 (81)	tr.	1.00 (59)	0.51 (35)	0.37 (18)	1.80 (55)	1.56 (45)
Total	104.70 (318)	109.18 (36)	106.46 (79)	107.90 (132)	103.37 (119)	102.68 (248)	106.29 (143)	104.14 (296)	103.95 (93)	103.21 (137)	105.02 (103)
Total-(O=F)	99.16 (301)	101.50 (43)	101.07 (65)	101.66 (53)	98.02 (55)	97.03 (166)	99.88 (151)	99.36 (282)	98.24 (107)	98.80 (150)	100.12 (95)
Cation numbers *pfu*											
P	0.97 (0)	0.96 (1)	1.01 (0)	0.99 (2)	1.00 (3)	0.99 (3)	1.00 (2)	1.00 (2)	0.98 (1)	1.02 (0)	1.03 (1)
Al	1.04 (0)	1.06 (1)	1.00 (1)	1.02 (3)	1.04 (2)	1.05 (2)	1.04 (2)	1.02 (2)	1.05 (2)	1.03 (1)	1.00 (1)
Na	1.00 (1)	1.01 (1)	0.95 (1)	0.96 (2)	0.89 (9)	0.92 (11)	0.89 (6)	0.94 (4)	0.96 (2)	0.81 (5)	0.83 (5)
F	1.16 (23)	1.62 (8)	1.10 (4)	1.29 (20)	1.13 (25)	1.22 (28)	1.35 (12)	0.99 (4)	1.21 (5)	0.91 (4)	1.00 (5)
Li*	tr.	bdl	0.05 (1)	0.04 (2)	0.11 (9)	tr.	0.11 (6)	0.06 (4)	0.04 (2)	0.19 (5)	0.17 (5)
Σ cat.	3.02 (0)	3.03 (1)	3.01 (0)	3.02 (1)	3.04 (1)	3.04 (2)	3.04 (1)	3.02 (1)	3.03 (1)	3.05 (2)	3.03 (1)
F/(F+OH)**	1.00 (0)	1.00 (0)	1.00 (0)	1.00 (0)	0.96 (9)	1.00 (1)	1.00 (0)	0.99 (2)	1.00 (0)	0.91 (4)	0.98 (2)

Cation numbers were calculated on the basis of nine positive charges.

* Li was calculated by difference to Na on the sodium site: Li = (1−Na).

** The low OH contents were calculated by difference to F in the fluorine site: OH = (1−F). Fluorine in MONT2-a and MONT10 was measured with time-zero integrated analysis.

TABLE 4. ELECTRON PROBE MICROANALYSES OF WARDITE, MORINITE, AND VITANIEMIITE

Sample	MONT9	MONT12	MONT12	MONT12	MONT12	MONT2	MONT2	MONT5
Phase	Wardite	Morinite	Morinite	Morinite	Morinite	Viitaniemiite	Viitaniemiite	Viitaniemiite
n	9	6	17	6	15	8	6	8
P_2O_5	36.10 (46)	28.14 (206)	28.27 (141)	29.74 (79)	29.46 (76)	30.28 (118)	27.66 (46)	29.65 (63)
Al_2O_3	37.27 (76)	21.26 (49)	21.01 (74)	21.15 (58)	20.59 (51)	21.92 (60)	21.76 (15)	20.16 (17)
FeO	n.a.	n.a.	n.a.	n.a.	n.a.	tr.	tr.	1.30 (36)
MgO	0.13 (8)	n.a.	n.a.	n.a.	n.a.	2.21 (38)	0.10 (2)	0.08 (4)
MnO	n.a.	n.a.	n.a.	n.a.	n.a.	3.42 (29)	2.25 (42)	14.05 (101)
CaO	0.52 (53)	22.42 (49)	22.33 (52)	22.72 (20)	22.79 (47)	16.89 (129)	21.70 (70)	9.67 (118)
Na_2O	7.24 (35)	3.69 (28)	4.96 (27)	5.89 (19)	6.15 (15)	12.90 (28)	11.79 (16)	12.07 (44)
F	0.79 (17)	14.56 (56)	16.23 (92)	16.74 (160)	17.19 (99)	17.41 (72)	19.56 (61)	15.33 (62)
H_2O*	17.56 (71)	15.89 (327)	13.80 (258)	10.19 (189)	10.37 (145)	3.16 (38)	1.66 (20)	3.57 (36)
Total	99.61 (37)	105.96 (120)	106.60 (68)	106.44 (56)	106.56 (58)	108.22 (137)	106.50 (112)	106.04 (127)
Total-(O=F)	99.28 (36)	99.83 (112)	99.77 (53)	99.38 (47)	99.32 (56)	100.89 (121)	98.26 (86)	99.58 (133)
Cation numbers *pfu*								
P	2.05 (2)	2.00 (8)	2.00 (4)	2.03 (3)	2.02 (3)	1.01 (2)	0.96 (1)	1.04 (1)
Al	2.94 (5)	2.11 (10)	2.06 (6)	2.00 (7)	1.97 (4)	1.02 (1)	1.05 (1)	0.99 (2)
Fe	n.a.	n.a.	n.a.	n.a.	n.a.	tr.	tr.	0.05 (1)
Mg	0.01 (1)	n.a.	n.a.	n.a.	n.a.	0.13 (2)	0.01 (0)	0.01 (0)
Mn	n.a.	n.a.	n.a.	n.a.	n.a.	0.11 (1)	0.08 (2)	0.49 (3)
Ca	0.04 (4)	2.02 (5)	1.99 (4)	1.96 (2)	1.98 (4)	0.71 (6)	0.96 (3)	0.43 (5)
Na	0.94 (5)	0.60 (5)	0.80 (3)	0.91 (2)	0.97 (2)	0.98 (1)	0.94 (1)	0.97 (3)
F	0.17 (4)	3.79 (11)	4.00 (8)	3.97 (15)	4.19 (12)	2.17 (9)	2.54 (6)	2.01 (9)
OH*	3.83 (4)	1.21 (11)	1.00 (8)	1.03 (15)	0.81 (12)	0.83 (9)	0.46 (6)	0.99 (9)
H_2O*	2.01 (19)	3.93 (118)	3.45 (94)	2.41 (42)	2.49 (40)	n.a.	n.a.	n.a.
Σ cat.	5.99 (3)	6.75 (7)	6.88 (5)	6.92 (2)	6.98 (4)	3.98 (4)	4.00 (2)	3.98 (2)
F/(F+OH)	0.04 (1)	0.76 (2)	0.80 (2)	0.79 (3)	0.84 (2)	0.72 (3)	0.85 (2)	0.67 (3)

Wardite calculated on the basis of 20 positive charges. * Hydroxyl groups calculated by difference on hydroxyl site: OH = (4−F).
Morinite calculated on the basis of 21 positive charges. * Hydroxyl groups calculated by difference on fluorine site: OH = (5−F).
Viitaniemiite calculated on the basis of 11 positive charges. * Hydroxyl groups calculated by difference on fluorine site: OH = (3−F).
H_2O calculated by difference between total measured and calculated hydroxyl groups.

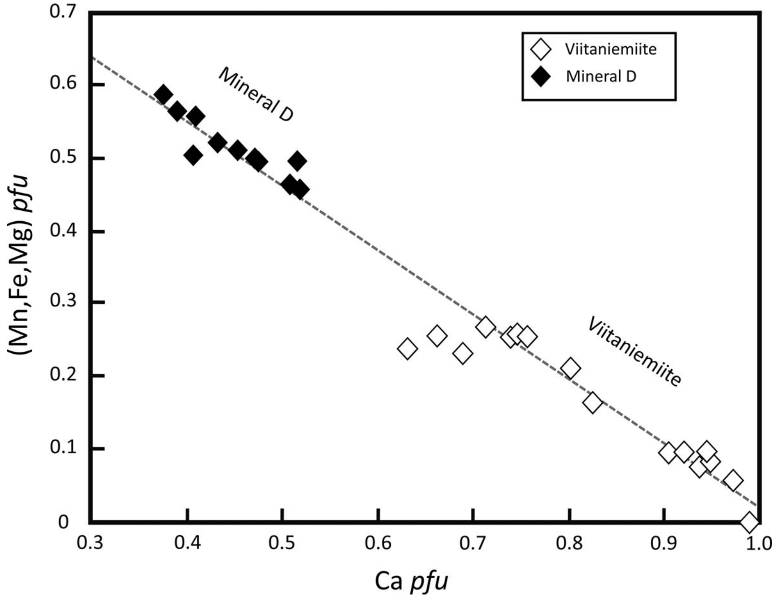

FIG. 7. Correlation between Ca per formula unit (*pfu*) and (Mn, Fe, Mg) *pfu* in viitaniemiite and in "Mineral D".

very intense, but clear zonation growth is visible with pink, orange, and brown colors appearing in crusts (Fig. 6d). Some samples present mineral phases visually similar to morinite, but a detailed analysis (cathodoluminescence, EPMA) showed that these phases are actually constituted by fibrous sodium-bearing fluorapatite (Fig. 6e). Electron probe microanalyses show a decrease in sodium (0.60 to 0.97 Na per formula unit) from the inside to the outside of the morinite crusts. Average composition is $Na_{0.94}Ca_{1.97}Mg_{0.01}Al_{1.97}(PO_4)_{2.04}(F_{4.26}OH_{0.43})\cdot 2H_2O$ (Table 4). Substitutions mentioned by Čech & Povondra (1985) have not been observed in our samples.

Viitaniemiite, $Na(Ca,Mn)Al(PO_4)(F,OH)_3$, is a rare mineral that occurs in Montebras as a colorless phase in altered amblygonite. It is pervasively mixed with lacroixite as rare patches of hundreds of microns in diameter. Viitaniemiite is recognizable in cathodoluminescence with a brown-orange (Fig. 3a$_3$) to red color of medium intensity (Fig. 6a). Studies on doped synthetic viitaniemiite suggest that REE and Mn^{2+} could be responsible for such a hue (Nagaraja *et al.* 2017, Pushpa Manjari *et al.* 2014). EPMA shows a Mn-Mg-bearing viitaniemiite with the following composition: $Na_{0.93}(Ca_{0.82}Mn_{0.09}Mg_{0.07})Al_{1.03}(PO_4)_{0.99}(F_{2.30}OH_{0.72})$ (Table 4). Changes in cathodoluminescent colors can be correlated with homovalent $Ca^{2+} = (Mn,Mg)^{2+}$ and heterovalent $2Na^{+} = (Ca,Mn,Mg)^{2+}$ substitution mechanisms (Shirose & Uehara 2014, Petrík *et al.* 2011, Lathi 1981). The first substitution leads to a viitaniemiite where manganese is more abundant than calcium (Fig. 7).

The phase called "Mineral D" shows a simplified chemical composition $Na(Mn,Ca)Al(PO_4)(F,OH)_3$, and although it seems to be a Mn-rich viitaniemiite, this phase was found in a different assemblage. It occurs as inclusions (250 μm) in eosphorite and shows a low relief and a very low birefringence. Textures seem to indicate that it is produced by alteration of eosphorite. Electron probe microanalyses give the empirical formula $Na_{0.96}(Mn_{0.49}Ca_{0.42}Fe_{0.04}Mg_{0.01})Al_{0.97}(PO_4)_{1.03}(F_{1.98}OH_{0.73})$ (Table 4). This composition seems to be part of a viitaniemiite solid solution involving the substitution mechanism $Ca^{2+} = (Mn, Fe, Mg)^{2+}$ (Fig. 7), only partly evidenced in a Carpathians quartz vein (Stevko *et al.* 2015) and in Namibia (Pirard & Hatert, *in prep.*).

Ca-bearing phosphates

Fluorapatite, $Ca_5(PO_4)_3F$, is a common mineral that occurs at all post-magmatic crystallization stages. It has been observed as euhedral crystals, as veins (with quartz and lacroixite), or as radiating masses or microscopic inclusions in montebrasite, crandallite, cassiterite, wavellite, and turquoise. Fluorapatite has a very bright cathodoluminescence in orange-yellow to yellow greenish hues (545 to 580 nm) (Fig. 6b, e). X-ray powder diffraction, infrared, and EPMA data clearly show that fluorapatites are invariably near the F-rich endmember. Manganese contents range from 0.4 to 3 wt.% MnO, while iron rarely reaches 0.4 wt.% FeO. Fluorapatite associated with morinite and

TABLE 5. ELECTRON PROBE MICROANALYSES OF FLUORAPATITE

Sample	MONT9	MONT9	MONT9	MONT9	MONT12	MONT12	MONT12
Phase		brown CL					
n	9	5	3	2	4	10	8
P_2O_5	41.96 (111)	41.88 (89)	41.49 (130)	43.39 (24)	42.14 (54)	40.18 (83)	40.78 (77)
Al_2O_3	tr.	0.13 (10)	tr.	bdl	0.11 (5)	0.17 (11)	0.22 (15)
FeO	0.34 (27)	0.33 (10)	0.36 (0)	tr.	0.10 (8)	tr.	tr.
MnO	2.99 (64)	1.24 (36)	1.93 (25)	0.77 (8)	1.04 (54)	0.43 (45)	0.44 (35)
CuO	bdl	bdl	bdl	bdl	0.17 (11)	bdl	bdl
CaO	51.58 (120)	53.44 (130)	52.39 (62)	53.13 (67)	52.84 (48)	53.80 (104)	53.49 (122)
Na_2O	bdl	bdl	bdl	bdl	0.19 (11)	0.41 (35)	tr.
F	3.56 (30)	4.26 (38)	2.52 (60)	4.64 (20)	4.61 (26)	4.06 (24)	4.33 (77)
Total	100.47 (135)	101.12 (89)	98.71 (78)	102.07 (99)	101.19 (62)	99.07 (147)	99.42 (166)
Total-(O=F)	98.97 (138)	99.32 (95)	97.65 (103)	100.12 (91)	99.25 (58)	97.37 (148)	97.60 (137)
Cation numbers *pfu*							
P	3.03 (5)	3.00 (3)	3.01 (4)	3.07 (1)	3.03 (2)	3.00 (4)	2.98 (3)
Al	tr.	0.02 (1)	tr.	tr.	tr.	tr.	0.02 (1)
Fe	tr.	bdl	tr.	bdl	tr.	bdl	bdl
Mn	0.22 (5)	0.09 (2)	0.14 (2)	0.05 (1)	0.07 (4)	0.04 (2)	tr.
Cu	bdl	bdl	bdl	bdl	bdl	0.01 (0)	bdl
Ca	4.71 (10)	4.89 (8)	4.82 (11)	4.76 (2)	4.81 (5)	4.96 (11)	5.03 (8)
Na	tr.	tr.	0.01 (0)	0.01 (0)	0.05 (2)	0.07 (4)	0.13 (3)
F	0.96 (8)	1.03 (2)	0.69 (18)	1.23 (4)	1.24 (7)	1.11 (9)	1.12 (7)
OH*	0.06 (6)	bdl	0.31 (18)	0.17 (468)			
Σ cat.	8.00 (6)	8.02 (2)	8.02 (8)	3.03 (101)	8.02 (5)	8.10 (4)	8.19 (4)
F/(F+OH)	0.96 (0)	1.00	0.69	1.00	0.96	1.00	1.00

Cation numbers calculated on 25 positive charges.

* Hydroxyl groups calculated by difference on fluorine site: OH = (1−F).

wardite shows up to 1 wt.% Na_2O and 0.5 wt.% Al_2O_3 (Table 5).

Minerals of the crandallite–goyazite solid solution, $(Ca,Sr)Al_3(PO_4)_2(OH)_5 \cdot H_2O$, are common alteration phases and show extensive substitutions at the Ca-Sr-Ba-REE site. Barium-poor crandallite and goyazite are very common and occur as veinlets associated with most other phosphates. Morinite frequently shows numerous inclusions of zoned euhedral rhombohedra of Ba-free crandallite–goyazite (Fig. 6c). Crandallite-group minerals are not cathodoluminescent, probably due to the absence of manganese and the relatively poor FeO contents (up to 1 wt.% FeO), which would act as a luminescence quencher. The variations of crandallite-group mineral compositions show a complete solid solution between the Ca and Sr endmembers (Figs. 6f and 8a), while the substitution toward Ba is very limited (less than 6% of the divalent site, Fig. 8a). The limited solid solution of crandallite–goyazite (trigonal, $R\overline{3}m$) toward gorceixite (monoclinic, *Cm*) is in good agreement with the arguments of Liferovich et *al.* (1999), who suggest that the different crystal systems of these minerals predetermine the limited isomorphism, although a partial solution between Sr and Ba has been observed by Baldwin *et al.* (2000).

Gorceixite, $BaAl_3(PO_4)(PO_3OH)(OH)_6$, occurs in more highly altered zones than crandallite–goyazite. It is generally associated with kaolinite and forms cryptocrystalline crusts. The average composition obtained by EPMA for this mineral is $(Ba_{0.97}Ca_{0.04}Sr_{0.02})Al_{2.96}Fe_{0.05}(PO_4)(PO_3OH)F_{1.04}(OH)_{5.95} \cdot 1.53H_2O$ (Table 6). The high fluorine content is a common feature of gorceixite, as observed in the nearby locality of Echassières (Nicolas & de Rosen 1963) and in several other places (Taylor *et al.* 1984, Milton *et al.* 1958, White 1981). A possible mechanism supporting this observation is $(Ca,Sr)^{2+} + OH^- = Ba^{2+} + F^-$, although more data would be required to validate this substitution (Fig. 8b).

Other phosphates

Variscite, $AlPO_4 \cdot 2H_2O$, is a common cryptocrystalline cream-colored phase forming an intimate mixture with kaolinite, wavellite, and quartz on the outer part of most samples (Fig. 9a). It is not easily observed under the

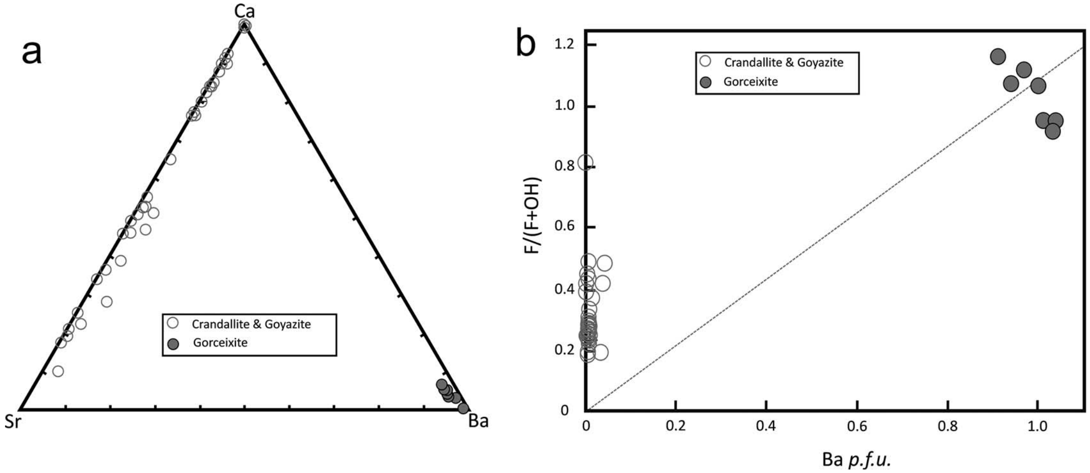

FIG. 8. (a) Variations of chemical compositions for crandallite-group minerals in the Ca–Sr–Ba ternary field. (b) Correlation between the barium and fluorine concentrations in gorceixite and Ba-rich crandallite–goyazite of Montebras.

optical microscope, and cathodoluminescence methods do not make it possible to differentiate the fine-grained mixtures formed of quartz, wavellite, and variscite. In our samples, the occasional green color of variscite-rich assemblages is probably due to the presence of turquoise and possibly of minerals such as "barrandite" (= aluminum-bearing strengite) and dufrénite (Lacroix 1910).

Wavellite, $Al_3(PO_4)_2(OH,F)_3 \cdot 5H_2O$, forms characteristic acicular aggregates, crusts, and independent needles up to 5 mm long (Fig. 9b). It is associated with many alteration phases and has been observed in direct contact with amblygonite in some samples. The average chemical composition of this species is $Al_{2.93}Fe_{0.01}(PO_4)_{2.04}(OH_{2.12}F_{0.88}) \cdot 5.04H_2O$ (Table 7).

Turquoise, $CuAl_6(PO_4)_4(OH)_8 \cdot 4H_2O$, is a very common mineral in Montebras, giving bluish to greenish colors to altered masses of phosphates (Fig. 9b). Textures vary from massive crusts to vesicular assemblage with wavellite, variscite, and kaolinite. Electron probe microanalyses in massive turquoise veins give the following composition: $Cu_{0.88}Fe_{0.02}Ca_{0.02}Al_{5.97}(PO_4)_{4.03}(OH_{7.24}F_{0.41}) \cdot 4.00H_2O$ (Table 7).

Triplite, Mn_2PO_4F, is an uncommon microscopic phase with a chemical composition $(Mn_{1.90}Fe_{0.04}Ca_{0.03})(PO_4)_{1.02}(F_{1.00}OH_{0.02})$ (Table 8). Eosphorite, $MnAlPO_4(OH)_2 \cdot H_2O$, occurs as yellowish inclusions in amblygonite and in some quartz veins where it forms subhedral crystals up to 1 mm in length. As mentioned before, eosphorite grains are frequently replaced by "Mineral D", which seems to be a Mn-rich viitaniemiite. The average chemical analysis of eosphorite is $(Mn_{0.68}Fe_{0.28}Ca_{0.01})Al_{0.98}(PO_4)_{1.02}(OH_{1.96}F_{0.04})_{2.00} \cdot 1.06H_2O$ (Table 8), corresponding to a Fe-rich composition. The $Mn^{2+} = (Fe, Ca)^{2+}$ substitution extends from 0.64 to 0.76 Mn *pfu*.

In lacroixite-fluorapatite veins cross-cutting viitaniemiite-bearing amblygonite, "F-phase" is observed as large colorless patches reaching 100 × 400 μm (Fig. $3a_1$). No pleochroism is observed and birefringence is extremely low (~0.001) (Fig. $3a_2$). In cathodoluminescence, the "F-phase" shows a bright vermilion color (Fig. $3a_3$, 10). Electron probe microanalyses (WDS and EDS) show a very high content in fluorine (up to 56 wt.% F) and an empirical chemical formula of $Na_{0.99}(Al_{0.77}P_{0.23})(F_{3.44}OH_{0.55})$, based on four anions (Table 9). The synthetic compound $NaAlF_4$, which could correspond to "F-phase", also shows a low birefringence and a very low refractive index (Liu *et al.* 2011), but it is known to be metastable at room temperature, at which it decomposes into chiolite and AlF_3, and it melts at higher temperatures (>500 °C) (Bjorseth *et al.* 1986, Zaitseva *et al.* 2009). The significant presence of phosphorus (~13 wt.% P_2O_5) and the very low birefringence (possibly isotropic) suggest that this phase could be a Na-Al fluoride xerogel in which it is known that phosphorus (as PO_4 groups) has complete solubility (Thisted *et al.* 2006, Kucharik & Vasiljev 2008). Regardless of the exact nature of this phase, the association of sodium aluminofluoride with phosphates could form in a setting petrologically analogous to the cryolite-viitaniemiite association observed in Francon Quarry, Quebec (Tarassoff *et al.* 2006, Ramik *et al.* 1983).

CHARACTERIZATION OF NON-PHOSPHATE MINERALS

Quartz is very common in Montebras, occurring as a late phase forming veins and filling cavities between phosphate crystals (Fig. 9a). However, in the quartz-rich

TABLE 6. ELECTRON PROBE MICROANALYSES OF CRANDALLITE-GROUP MINERALS

Sample	MONT7	MONT7	MONT9	MONT12	MONT12	MONT12	MONT12	MONT12	MONT12
Phase	Gorceixite	Gorceixite	Goyazite	Crandallite	Crandallite	Goyazite	Crandallite	Goyazite	Goyazite
n	5	3	3	5	7	3	4	5	2
P_2O_5	25.78 (26)	26.33 (49)	32.55 (98)	29.40 (43)	27.76 (143)	27.40 (327)	29.22 (284)	23.48 (102)	26.77 (85)
Al_2O_3	27.73 (15)	27.38 (30)	32.65 (77)	34.06 (33)	35.56 (61)	32.42 (111)	37.54 (444)	31.96 (129)	33.22 (45)
FeO	0.59 (21)	0.85 (66)	bdl	bdl	bdl	bdl	bdl	bdl	0.04 (1)
MnO	bdl	bdl	bdl	bdl	bdl	0.13 (12)	bdl	bdl	bdl
CuO	0.17 (4)	0.08 (4)	bdl	0.13 (5)	bdl	0.06 (3)	bdl	0.07 (3)	0.14 (11)
CaO	0.58 (9)	0.26 (19)	5.64 (77)	6.58 (42)	11.04 (45)	3.37 (196)	12.90 (101)	2.68 (48)	5.58 (30)
SrO	0.52 (3)	0.32 (22)	11.57 (159)	10.99 (53)	3.34 (168)	15.98 (145)	0.63 (126)	18.10 (32)	12.00 (99)
BaO	26.72 (91)	28.68 (25)	1.31 (26)	0.28 (18)	bdl	bdl	bdl	0.19 (24)	bdl
Na_2O	0.07 (2)	0.09 (3)	bdl	0.04 (3)	bdl	0.01 (0)	bdl	bdl	0.03 (1)
K_2O	0.22 (5)	0.11 (8)	bdl	bdl	bdl	bdl	bdl	bdl	bdl
F	3.83 (14)	3.24 (5)	1.56 (68)	1.15 (4)	1.14 (37)	2.34 (219)	1.09 (12)	1.34 (27)	1.30 (25)
H_2O*	15.51 (53)	13.74 (124)	14.13 (82)	18.89 (85)	23.79 (300)	20.11 (571)	21.46 (732)	25.74 (162)	23.14 (162)
Total	102.17 (22)	101.71 (32)	99.77 (83)	101.67 (17)	103.00 (55)	102.46 (125)	103.05 (46)	103.78 (77)	102.56 (45)
Total O=F	100.55 (25)	100.35 (33)	99.11 (64)	101.19 (18)	102.52 (68)	101.47 (203)	102.60 (41)	103.21 (73)	102.02 (35)
Cation numbers *pfu*									
P	1.99 (2)	2.02 (1)	2.07 (5)	1.92 (1)	1.82 (5)	1.89 (16)	1.82 (1)	1.74 (6)	1.85 (3)
Al	2.98 (2)	2.93 (4)	2.89 (8)	3.10 (4)	3.25 (11)	3.13 (19)	3.26 (6)	3.31 (12)	3.20 (9)
Fe	0.05 (2)	0.06 (5)	bdl	bdl	bdl	bdl	bdl	bdl	0.00 (0)
Mn	bdl	bdl	bdl	bdl	bdl	0.01 (1)	bdl	bdl	bdl
Cu	0.02 (1)	bdl	bdl	bdl	bdl	0.01 (0)	bdl	0.01 (0)	0.02 (1)
Ca	0.06 (1)	0.03 (2)	0.45 (6)	0.54 (3)	0.92 (3)	0.30 (18)	1.02 (2)	0.25 (4)	0.49 (2)
Sr	0.03 (0)	0.02 (1)	0.50 (7)	0.49 (3)	0.15 (7)	0.76 (5)	0.03 (6)	0.92 (2)	0.57 (4)
Ba	0.96 (3)	1.02 (1)	0.04 (1)	bdl	bdl	bdl	bdl	bdl	0.01 (1)
Na	0.01 (0)	0.02 (1)	bdl	0.01 (0)	bdl	bdl	bdl	bdl	0.01 (0)
K	0.03 (1)	bdl	bdl	bdl	bdl	bdl	bdl	bdl	bdl
F	1.11 (4)	0.93 (2)	0.37 (16)	0.28 (1)	0.28 (8)	0.59 (53)	0.25 (1)	0.37 (8)	0.34 (7)
OH*	3.89 (4)	4.07 (2)	4.63 (16)	4.72 (1)	4.72 (8)	4.41 (53)	4.75 (1)	4.63 (8)	4.66 (7)
H_2O**	2.78 (18)	2.12 (41)	1.23 (27)	2.51 (25)	3.81 (87)	3.32 (147)	3.07 (217)	5.23 (62)	3.98 (56)
Σ (Ca,Sr,Ba)	1.04 (3)	1.06 (4)	1.00 (1)	1.05 (3)	1.07 (8)	1.07 (14)	1.05 (7)	1.18 (5)	1.07 (5)
F/(F+OH)	0.22 (1)	0.19 (0)	0.07 (3)	0.06 (0)	0.06 (2)	0.12 (11)	0.05 (0)	0.07 (2)	0.07 (1)

Cation numbers were calculated on the basis of 21 positive charges.

* Hydroxyl groups were calculated by difference on the fluorine site: OH = (5−F).

** H_2O calculated by difference between the total measured and calculated hydroxyl groups.

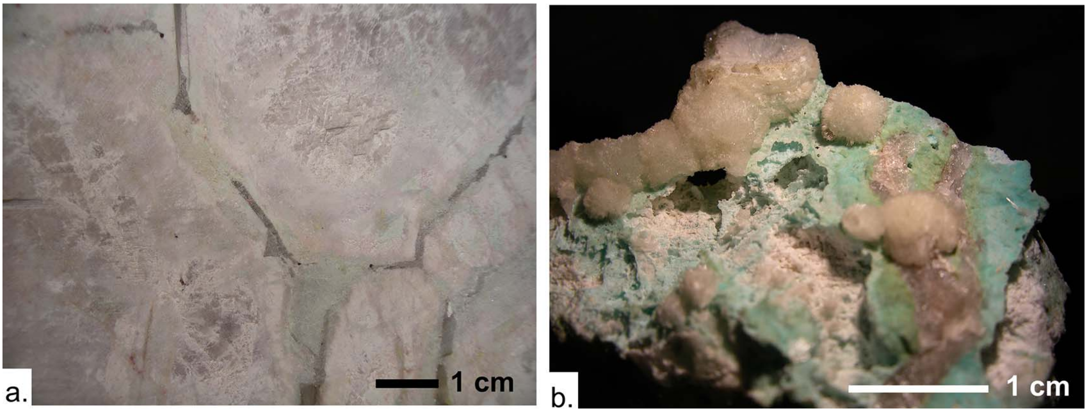

FIG. 9. (a) Macroscopic view of amblygonite (gray) altered to kaolinite + crandallite (white zones), cross-cut by quartz veins surrounded by variscite and wavellite (greenish) (sample MONT4). (b) Macroscopic sample showing radial acicular aggregates of wavellite, associated with alteration phases such as kaolinite/variscite (white) and turquoise (bluish to greenish).

TABLE 7. ELECTRON PROBE MICROANALYSES OF WAVELLITE AND TURQUOISE

Sample	MONT13	MONT15	MONT5	MONT3
Phase	Wavellite	Wavellite	Turquoise	Turquoise
n	2	2	3	2
P_2O_5	34.88 (72)	34.58 (67)	33.65 (205)	33.70 (94)
Al_2O_3	35.66 (60)	35.56 (22)	34.66 (140)	34.97 (141)
FeO	0.10 (3)	0.08 (6)	0.09 (7)	2.16 (44)
MnO	bdl	0.11 (3)	n.a.	n.a.
CuO	bdl	0.08 (7)	4.36 (259)	5.26 (77)
CaO	0.03 (1)	bdl	0.62 (51)	1.21 (83)
Na_2O	bdl	bdl	bdl	0.57 (48)
K_2O	0.07 (4)	0.15 (3)	0.16 (3)	0.12 (2)
F	3.96 (4)	4.00 (22)	1.11 (28)	2.23 (22)
H2O**	26.05 (71)	26.47 (117)	23.78 (471)	20.25 (23)
Total	100.98 (56)	101.14 (12)	99.51 (130)	100.63 (102)
Total-(O=F)	99.32 (54)	99.46 (21)	99.04 (121)	99.69 (112)
Cation numbers *pfu*				
P	2.05 (4)	2.04 (1)	4.17 (17)	4.07 (13)
Al	2.92 (6)	2.93 (2)	5.99 (21)	5.88 (21)
Fe	0.01 (0)	bdl	bdl	0.26 (5)
Mn	bdl	0.01 (0)	n.a.	n.a.
Cu	bdl	bdl	0.47 (26)	0.57 (8)
Ca	bdl	bdl	0.10 (8)	0.19 (13)
Na	bdl	bdl	bdl	0.16 (13)
K	0.01 (0)	0.01 (0)	0.03 (1)	0.02 (0)
F	0.87 (1)	0.88 (4)	0.52 (15)	1.01 (10)
OH*	2.13 (1)	2.12 (4)	7.48 (15)	6.99 (10)
H_2O**	4.97 (19)	5.11 (34)	7.98 (291)	6.14 (20)
Σ cat.	4.99 (2)	5.01 (2)	10.81 (23)	11.13 (22)
F/(F+OH)	0.29 (0)	0.29 (1)	0.06 (2)	0.13 (1)

Wavellite calculated on 19 positive charges. * Hydroxyl groups calculated by difference on hydroxyl site: OH = (3−F).
Turquoise calculated on 40 positive charges. * Hydroxyl groups calculated by difference on hydroxyl site: OH = (8−F).
** H_2O calculated by difference between total measured and calculated hydroxyl groups.

TABLE 8. ELECTRON PROBE MICROANALYSES OF EOSPHORITE AND TRIPLITE

Sample	MONT5	MONT5	MONT5	MONT2
Phase	Eosphorite	Eosphorite	Eosphorite	Triplite
n	8	3	3	4
P_2O_5	31.41 (52)	31.31 (52)	31.81 (11)	32.23 (64)
SiO_2	0.04 (2)	0.05 (2)	0.04 (1)	bdl
Al_2O_3	21.57 (33)	21.41 (31)	21.95 (23)	0.04 (1)
FeO	8.54 (75)	9.88 (113)	8.01 (122)	1.96 (8)
MnO	20.86 (67)	20.49 (150)	21.83 (90)	59.99 (53)
CuO	bdl	bdl	0.10 (4)	n.a.
MgO	bdl	bdl	bdl	bdl
CaO	0.40 (9)	0.20 (4)	0.06 (1)	0.71 (1)
SrO	bdl	bdl	bdl	0.10 (2)
BaO	bdl	bdl	bdl	bdl
Na_2O	bdl	bdl	0.08 (1)	bdl
F	0.54 (32)	0.13 (23)	0.12 (14)	8.50 (45)
H_2O*	16.07 (75)	15.88 (98)	15.31 (17)	bdl
Total	99.64 (34)	99.58 (29)	99.44 (11)	103.62 (102)
Total-(O = F)	99.41 (26)	99.53 (22)	99.38 (14)	100.04 (100)
Cation numbers *pfu*				
P	1.02 (1)	1.02 (1)	1.02 (1)	1.02 (1)
Si	bdl	bdl	bdl	bdl
Al	0.98 (2)	0.97 (2)	0.98 (1)	bdl
Fe	0.27 (3)	0.32 (4)	0.25 (4)	0.04 (0)
Mn	0.68 (2)	0.67 (4)	0.70 (3)	1.90 (2)
Cu	bdl	bdl	bdl	n.a.
Mg	bdl	bdl	bdl	bdl
Ca	0.02 (0)	0.01 (0)	bdl	0.03 (0)
Sr	bdl	bdl	bdl	bdl
Ba	bdl	bdl	bdl	bdl
Na	bdl	bdl	0.01 (0)	bdl
F	0.07 (4)	0.02 (3)	0.01 (2)	1.00 (5)
OH*	1.93 (4)	1.98 (3)	1.99 (2)	0.02 (2)
H_2O**	1.10 (11)	1.05 (16)	0.95 (4)	
Σ cat.	2.99 (1)	3.00 (0)	2.98 (0)	2.99 (0)
F/(F+OH)	0.03 (2)	0.01 (1)	0.01 (1)	0.98 (0)

Eosphorite calculated on ten positive charges. * Hydroxyl groups calculated by difference on hydroxyl site (2−F).

Triplite calculated on nine positive charges. * Hydroxyl groups calculated by difference on fluorine site (1−F).

** H_2O calculated by difference between total measured and calculated hydroxyl groups.

zones of the pegmatite, its abundance indicates precipitation at an earlier stage. By contrast to feldspars (microcline and albite), muscovite is a common phase in all phosphate pods. It shows lamellae reaching 0.1 to 10 mm in amblygonite and is often rimmed by fluorapatite. Chemical composition suggests that the lithium content of muscovite can reach 0.12 atoms *pfu* (Table 10), which is consistent with its infrared spectrum. However, no lepidolite micas have been observed in Montebras in the scope of this study, despite the description of polylithionite and zinnwaldite in other parts of the deposit (Marcoux *et al.* 2021).

Kaolinite is very frequent in altered phosphate pods of Montebras and sometimes occurs as a diffuse cement between masses of amblygonite–montebrasite. Its dark blue cathodoluminescence color makes it recognizable from turquoise and variscite, which do not show any luminescence. Its chemical composition is ideal, although infrared spectroscopy shows contamination by residual particles of micas that are not visible in optical microscopy (Table 10).

Cassiterite is a common phase observed in all samples. Grains are yellowish to brown, subhedral, and disseminated

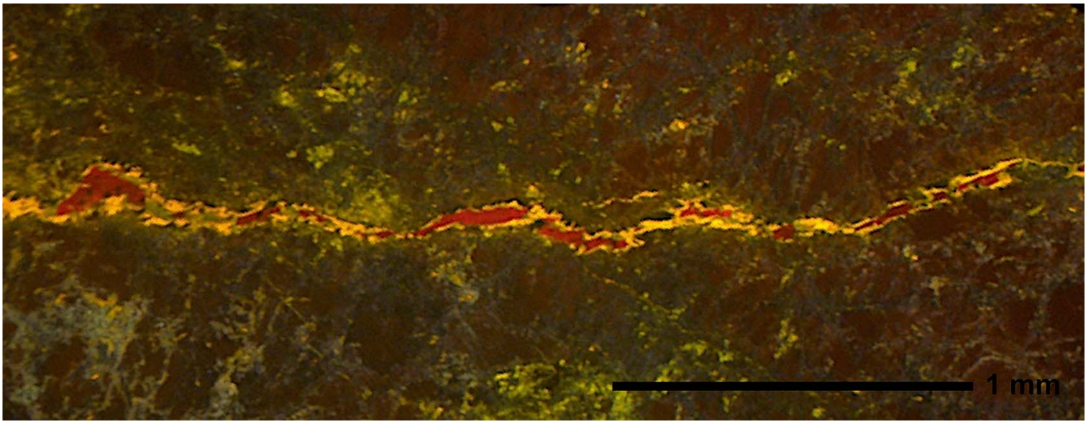

FIG. 10. Vein of the "F-phase" (bright red) surrounded by secondary lacroixite (yellow), cross-cutting amblygonite–montebrasite (sample MONT2, CL microscopy).

in phosphate pods. Small trails of kidney-shaped grains, with colors ranging from yellow to orange-brown, sometimes almost opaque, occur in some quartz veins (Fig. 11b). These grains show an important zonation and a complex convoluted internal texture. Darker grains with similar features are also found as rims around stannoidite (Fig. 11a). The chemical analysis indicates that these grains correspond to a Fe-rich (up to 35% substitution for Sn) cassiterite with minor concentrations of Cu, Nb, and Ta. These chemical properties, the gel-like textures (Fig. 11c), and the X-ray powder diffraction pattern not entirely consistent with that of cassiterite suggest that this mineral phase is varlamoffite. Hübnerite and tantalite-(Mn) with ixiolite *s.l.*, in small dark lamellae, have also been observed in altered zones (Fig. 11d).

Finally, considering the subject of this paper, the following minerals are mentioned in the scientific literature related to phosphate-bearing lithological facies of Montebras. Dufrénite is described as micro-inclusions in variscite, while libethenite occurs on feldspar crystals (Lacroix 1910). Torbernite (as well as cuprite) are associated with tin-rich masses (Lacroix 1901, 1910), and late veins of baryte, fluorapatite, fluorite, and autunite are common (Aubert 1969, Marcoux *et al.* 2021).

The phosphate-rich masses in the quartz-rich zones are described as occasionally containing lepidolite (Lacroix 1895), while the pegmatite contains polylithionite–zinnwaldite (Marcoux *et al.* 2021). This pegmatitic facies is also rich in Sn-W-Nb-Ta mineralization expressed as wolframite, scheelite, qitianlingite, mawsonite, stannite, tennantite subgroup minerals, löllingite, arsenopyrite, chalcopyrite, galena, vinciennite, covellite, bornite, and alteration products malachite, chrysocolla, and scorodite, not observed in this study (Lacroix 1901, Aubert 1969, Marcoux *et al.* 2021).

TABLE 9. ELECTRON PROBE MICROANALYSES OF "F-PHASE"

Sample	MONT2	MONT2	MONT2
Phase			F-correction
n	7	6	8
P_2O_5	13.30 (72)	12.86 (36)	12.23 (87)
Al_2O_3	27.49 (45)	27.29 (19)	37.15 (115)
FeO	0.05 (3)	bdl	n.a. (0)
MgO	0.02 (1)	bdl	n.a. (0)
MnO	0.13 (2)	0.13 (6)	0.08 (4)
CuO	bdl	bdl	n.a. (0)
CaO	0.16 (3)	0.27 (26)	0.19 (4)
Na_2O	25.29 (33)	24.58 (29)	23.49 (134)
F	56.35 (87)	53.94 (82)	46.98 (76)
H_2O*	2.21 (62)	3.93 (33)	11.01 (233)
Total	125.12 (96)	123.07 (19)	120.13 (199)
Total-(O = F)	101.40 (78)	100.36 (29)	100.35 (179)
Cation numbers *pfu*			
P	0.23 (1)	0.22 (1)	0.22 (1)
Al	0.67 (2)	0.65 (1)	0.95 (5)
Fe	bdl	bdl	n.a. (0)
Mg	bdl	bdl	n.a. (0)
Mn	bdl	bdl	bdl
Cu	bdl	bdl	n.a. (0)
Ca	bdl	bdl	bdl
Na	1.02 (2)	0.97 (1)	0.98 (7)
F	3.69 (8)	3.47 (5)	3.21 (11)
OH*	0.31 (8)	0.53 (5)	0.79 (11)
Σ cat.	1.93 (4)	1.85 (1)	2.16 (11)
F/(F+OH)	0.92 (2)	0.87 (1)	0.80 (3)

"F-phase" calculated on four anions (F+OH) optimized for an average of two cations.

* Hydroxyl groups calculated by difference on fluorine site for (4−F).

TABLE 10. ELECTRON PROBE MICROANALYSES OF SILICATES

Sample	MONT2	MONT12	MONT15	MONT15	MONT12	MONT12
Phase	Muscovite	Muscovite	Muscovite	Muscovite	Muscovite	Kaolinite
n	3	2	2	2	3	1
P_2O_5	0.04 (2)	bdl	tr.	tr.	bdl	bdl
SiO_2	46.51 (91)	45.98 (85)	45.68 (74)	45.40 (60)	45.88 (35)	42.81
Al_2O_3	36.73 (27)	36.14 (20)	36.14 (16)	35.82 (104)	36.08 (23)	37.84
FeO	bdl	0.52 (1)	0.63 (14)	0.71 (57)	0.72 (2)	0.08
MnO	0.07 (6)	tr.	0.26 (10)	0.18 (3)	0.11 (1)	0.10
CuO	0.07 (3)	tr.	0.09 (13)	tr.	tr.	0.07
MgO	0.03 (2)	0.16 (4)	0.06 (0)	0.06 (3)	0.13 (1)	tr.
CaO	0.06 (4)	tr.	bdl	tr.	0.04 (3)	0.05
SrO	bdl	tr.	0.03 (4)	bdl	bdl	bdl
BaO	bdl	0.08 (6)	bdl	bdl	0.07 (6)	0.15
Na_2O	0.15 (2)	0.33 (7)	0.26 (13)	0.38 (13)	0.34 (3)	tr.
K_2O	10.95 (13)	10.64 (32)	10.73 (4)	10.61 (42)	11.05 (6)	bdl
F	0.86 (2)	1.43 (26)	1.31 (8)	1.31 (6)	1.39 (5)	0.17
H_2O*	4.09 (6)	3.78 (7)	3.83 (7)	3.80 (2)	3.81 (2)	13.06
Total	99.62 (107)	99.43 (141)	99.09 (71)	98.72 (14)	99.72 (50)	94.37
Total-(O=F)	99.26 (107)	98.83 (130)	98.54 (75)	98.17 (16)	99.14 (48)	94.31
Cation numbers *pfu*						
P	bdl	bdl	bdl	bdl	bdl	bdl
Si	3.10 (2)	3.09 (2)	3.08 (3)	3.08 (4)	3.08 (0)	1.96
Al	2.88 (2)	2.86 (2)	2.87 (4)	2.86 (9)	2.86 (0)	2.05
Fe	bdl	0.03 (0)	0.04 (1)	0.04 (3)	0.04 (0)	bdl
Mn	bdl	bdl	bdl	0.01 (0)	0.01 (0)	bdl
Cu	bdl	bdl	bdl	bdl	bdl	bdl
Mg	bdl	0.02 (0)	0.01 (0)	0.01 (0)	0.01 (0)	bdl
Ca	bdl	bdl	bdl	bdl	bdl	bdl
Sr	bdl	bdl	bdl	bdl	bdl	bdl
Ba	bdl	bdl	bdl	bdl	bdl	bdl
Na	0.02 (0)	0.04 (1)	0.03 (2)	0.05 (2)	0.04 (0)	bdl
K	0.93 (2)	0.91 (4)	0.92 (0)	0.92 (3)	0.95 (1)	bdl
F	0.18 (1)	0.30 (5)	0.28 (2)	0.28 (1)	0.29 (1)	0.02
OH*	1.82 (1)	1.70 (5)	1.72 (2)	1.72 (1)	1.71 (1)	4.00
Σ cat.	6.95 (2)	6.98 (0)	6.98 (2)	6.99 (3)	7.00 (1)	4.03
F/(F+OH)	0.09 (0)	0.15 (3)	0.14 (1)	0.14 (1)	0.15 (0)	0.01

Micas calculated on 22 positive charges. * Hydroxyl groups calculated by difference on hydroxyl site (2−F).
Kaolinite calculated on 14 positive charges. * Hydroxyl groups calculated by difference on hydroxyl site (4−F).

DISCUSSION AND CONCLUSIONS

Cathodoluminescence applied to aluminum phosphates

Deciphering phosphate petrography is of prime interest to better assess pegmatite petrogenesis (Prado Araujo *et al.* 2023a). Iron-manganese phosphates, generally resulting from the transformation of primary minerals of the triphylite group (Rao *et al.* 2014, Lyalina *et al.* 2023), occur as various phases with bright colors under the microscope, thus making their identification relatively straightforward (Baijot *et al.* 2012, 2014). Most aluminum phosphates, however, are colorless mineral phases with similar relief (Fig. 3a_1, 3b_1) and low birefringence (Fig. 3a_2, 3b_2), making valuable observations and mineralogical, petrological, and textural interpretations based on thin sections very difficult. The lack of efficient distinction between aluminum phosphates by standard optical microscopy was recently bypassed by Prado Araujo *et al.* (2020), who determined the genetic sequences of aluminum phosphates from the Buranga pegmatite (Rwanda) using micro-Raman spectrometry (Prado Araujo *et al.* 2023a, b).

In the present paper, we demonstrated the efficiency of cathodoluminescence microscopy for complementing the classical petrographic observations of aluminum phosphates. Indeed, these colorless phases are totally appropriate

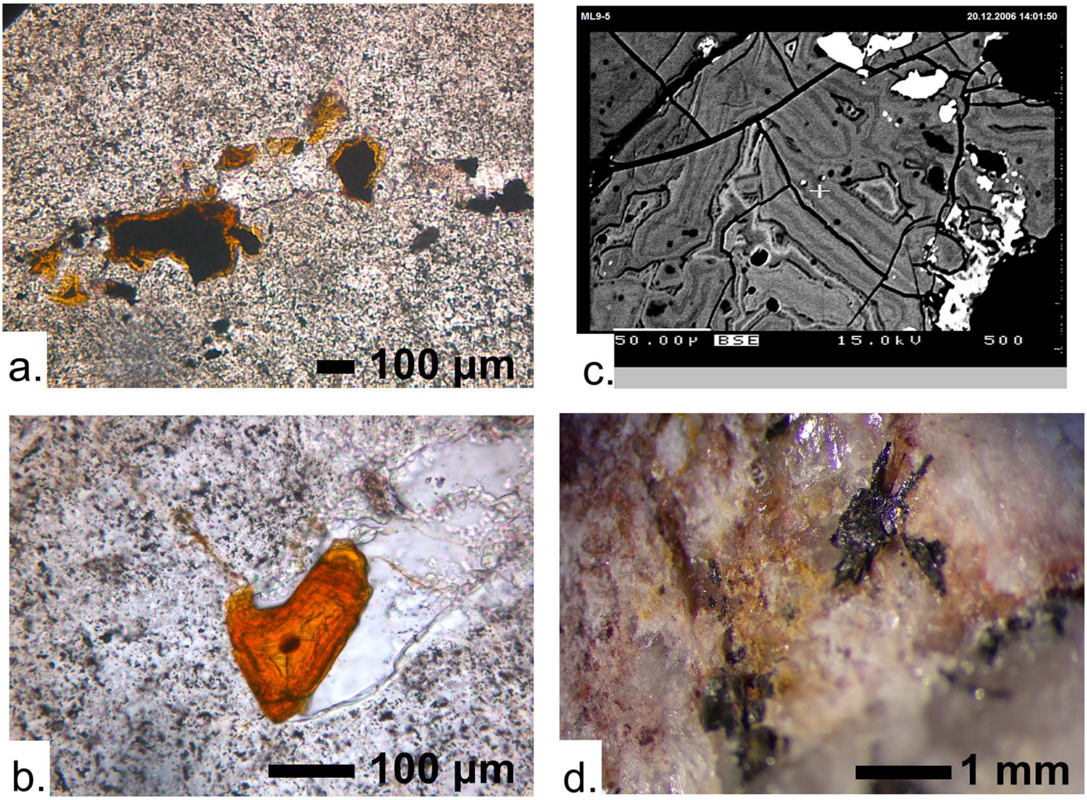

FIG. 11. (a) Grains of stannoidite (black), surrounded by rims of varlamoffite (brown), included in a mixture of quartz and amblygonite–montebrasite (plane-polarized light, sample MONT 9). (b) Inclusion of orange cassiterite (plane-polarized light, sample MONT9). (c) Zoned varlamoffite grain deposited around residual stannoidite (white) and altered fluorapatite (light gray) in montebrasite (black) in back-scattered electron microscopy (sample MONT9). (d) Small black lamellae of oxide minerals, constituted by hübnerite, tantalite-(Mn), and ixiolite *s.l.* (sample MONT8).

for CL techniques, since they show various luminescence colors under the electron beam and are mostly free of luminescence quenchers.

In the host primary phosphate of Montebras (amblygonite–montebrasite), a diffuse replacement by lacroixite, not always resolvable even with back-scattered electron imaging, was clearly observed in CL microscopy, since lacroixite produces very different light emission responses compared to minerals of the amblygonite–montebrasite solid solution. Different generations of amblygonite–montebrasite, as well as secondary replacement textures of lacroixite and apatite, can also be clearly distinguished using this technique (Fig. 5b). Finally, accessory phases, such as viitaniemiite, “Mineral D”, and an “F-phase”, which are discreet and undistinguishable in optical microscopy, show distinct colorful and bright cathodoluminescence responses, thus making the method very appropriate for the detection and textural analysis of such phases (Fig. 3a$_3$, 3b$_3$).

Trace element analysis of pegmatite phosphates

LA-ICP-MS is a powerful technique to determine the trace element contents in minerals, but it has rarely been applied to pegmatite phosphates. Roda-Robles *et al.* (2014) were the first authors to investigate the trace element contents of several series of iron-manganese phosphates, and they showed that, generally, these phases are poor in trace elements. In the triphylite–lithiophilite series [$LiFe^{2+}(PO_4)$–$LiMn^{2+}(PO_4)$], Zn is the main trace element, while Ca-bearing minerals of the graftonite–beusite-(Ca) solid solution [$Fe^{2+}Fe^{2+}_2(PO_4)_2$–$CaMn^{2+}_2(PO_4)_2$] are the richest in REE, and members of the triplite–zwieselite series [$Mn^{2+}_2(PO_4)F$–$Fe^{2+}_2(PO_4)F$] are enriched in Nb and Ta (Roda-Robles *et al*. 2014). More recently, Roda-Robles *et al.* (2020) investigated the trace element contents of iron-manganese phosphates from the Cañada (Salamanca, Spain) and Palermo #1 (New Hampshire, USA) pegmatites and concluded that the behavior of trace elements in these phases was constrained by crystal-chemical, geochemical, and geological factors. They were able, however, to satisfactorily use the phosphate trace element geochemistry to distinguish early primary (magmatic) phosphates from the late secondary assemblages. Roda-Robles *et al.* (2022, 2024) finally used the trace element contents of apatite-group minerals to distinguish the different generations of this phase in pegmatites, granites, and quartz veins from the Central Iberian Zone (Spain and Portugal), as well as in the Berry-Havey pegmatite (Maine, USA).

The present paper gives the first results of LA-ICP-MS analyses of aluminum phosphates of the amblygonite–montebrasite solid solution and of lacroixite. These preliminary data show the ability of the technique to differentiate several generations of phosphates, in good agreement with the CL and optical observations, as well as with the electron probe microanalyses. In the scope of this paper, the interpretation of trace element data is limited, but a more complete study of silicates and oxides occurring in the vicinity of phosphate nodules could provide useful information about the relationships between phosphates parageneses and the host rocks.

It must be underlined, however, that most samples investigated in our study were unsuitable for the LA-ICP-MS technique, since many seemingly clear, primary amblygonite–montebrasite samples showed significant contamination by solid and/or fluid inclusions. Such data therefore required a careful case-by-case processing of the original signal using the GLITTER software (Griffin *et al.* 2008). A comparison of the processed data of complex signals, with naturally clean analyses, showed that this removal procedure of contaminants was very efficient.

Petrogenesis of Montebras phosphates

The complexity of the amblygonite–montebrasite assemblages of Montebras is mostly the result of post-magmatic alteration processes. Although some minor mineral phases (topaz, Fe-Mn phosphates) could be of magmatic origin and associated with the formation of primary amblygonite, it appears that Na-bearing and most alkaline earth (Ca, Sr, Ba) minerals are the result of metasomatic and hydrothermal replacements and precipitations, while metal-free alumino-phosphates are linked to relatively low-temperature alteration processes.

The petrogenesis of phosphate pods of the Montebras pegmatite is more extensively developed in Pirard & Hatert (*in prep.*). The pegmatitic cupola has been formed by the residual melt of the microgranite, leading to a magma heavily enriched in alkaline elements (Na_2O, K_2O, and Li_2O), in fluorine, and in phosphorus. Extreme fractionation of this magma allowed the formation of the albite leucogranite, as well as an enrichment of the residual melt in F, P, B, Sn, Nb, and Ta. The formation of phosphate nodules could result from a possible melt–melt immiscibility, leading to a phosphorus- and fluorine-rich magmatic liquid characterized by a considerably low solidus. However, Prado Araujo *et al.* (2023a) consider, for the Buranga pegmatite, that the immiscibility process is unlikely, and that aluminum phosphate pods form at the crystallization front of a water- and flux-bearing residual pegmatitic melt, where the accumulation of incompatible elements creates a P-rich melt boundary layer. In Montebras, amblygonite and triplite are the primary phases crystallizing at this magmatic stage.

Crystallization of the magma leads to a separation between the residual melt and fluids enriched in fluorine that formed secondary fluorine-rich phases such as amblygonite or lacroixite. As the system further cooled down, other veins crystallized that contain an assemblage of quartz, micas, eosphorite, and fluorapatite. As the fluorine content in fluids gradually decreases, F-poor ternary montebrasite crystallizes in those veins. However, the fluorine levels are still high enough for a further precipitation of lacroixite, viitaniemiite, “Mineral D”, and eventually the “F-phase”.

Further cooling increases the calcium activity, and this element consequently becomes more involved in metasomatic reactions. Fluorapatite, mostly absent in the primary (magmatic) assemblage, becomes very frequent at this hydrothermal stage and precipitates in open cavities, where it replaces earlier phosphates. Na-Ca phosphates (morinite, wardite) would also appear during this stage, but further hydrothermal alteration processes often decompose these phases into apatite- and crandallite-group minerals. The seemingly frequent alteration of morinite and wardite into Na-rich fluorapatite could partly explain the rarity of these minerals in many deposits, where fluorapatite, crandallite, and hydrated aluminum phosphates are abundant.

Finally, magmatic silicates are altered into kaolinite during low-temperature hydrothermal processes, and more crandallite-group minerals are precipitated. The alteration of copper-bearing sulfide also permits the precipitation of turquoise. This late stage can be undistinguishable from meteoric alteration, although variscite and wavellite are probably formed essentially from indirect weathering.

ACKNOWLEDGMENTS

Many thanks are due to Dr. Lydie Touret, former curator of the ENSMP, for the loan of most samples, as well as to Heinz-Jürgen Bernhardt (Bochum) who performed the electron probe microanalyses, and to Eddy Poty (ULiège) who gave us access to the CL microcope. The two reviewers Pietro Vignola and Miguel Angel Galliski are acknowledged for their constructive comments.

References

Aubert, G. (1969) Les coupoles granitiques de Montebras et d'Echassières (Massif Central français) et la genèse de leur minéralisation étain-lithium-tungstène-béryllium. *Mémoire du BRGM* **46**, 354 pg. (in French).

Baijot, M., Hatert, F., & Philippo, S. (2012) Mineralogy and geochemistry of phosphates and silicates in the Sapucaia pegmatite, Minas Gerais, Brazil: Genetic implications. *The Canadian Mineralogist* **50**, 1531–1554.

Baijot, M., Hatert, F., Dal Bo, F., & Philippo, S. (2014) Mineralogy and petrography of phosphate mineral associations from the Jocão pegmatite, Minas Gerais, Brazil. *The Canadian Mineralogist* **52**, 373–397.

Balagny, C. (1939) *Le mystère de la callaïs*. Fontenay-le-Compte Imp., France, 48 pg.

Baldwin, J.R., Hill, P.G., von Knorring, O., & Oliver, G.J.H. (2000) Exotic aluminium phosphates, natromontebrasite, brazilianite, goyazite, gorceixite and crandallite from rare-element pegmatites in Namibia. *Mineralogical Magazine* **64**(6), 1147–1164.

Bjorseth, O., Herstad, O., & Holm, J.L. (1986) On the physical and thermodynamic stability of solid sodium tetrafluoroaluminate. *Acta Chemica Scandinavia* **A40**, 566–571.

Burnham, C.W. (1991) *LCLSQ version 8.4., Least-Squares Refinement of Crystallographic Lattice Parameters*. Harvard University Department of Earth and Planetary Sciences, Cambridge, Massachusetts, USA.

Čech, F. & Povondra, P. (1985) Identity of ježekite with morinite. *Bulletin de Minéralogie* **108**, 533–539.

Černá, I., Černý, P., & Ferguson, R.B. (1973) The fluorine content and some physical properties of the amblygonite–montebrasite minerals. *American Mineralogist* **58**, 291–301.

Černý, P. & Ercit, T.S. (2005) The classification of granitic pegmatites revisited. *The Canadian Mineralogist* **43**, 2005–2026.

Charoy, B. & Noronha, F. (1999) Rare-element (Li-rich) granitic and pegmatitic plutons: A primary or superimposed signature. *Revista Brasileira de Geociencias* **29**(1), 3–8.

Dias, I.N., Pinheiro, M.V.B., Moreira, R.L., Krambrock, K., Guedes, K.J., Menezes Filho, L.A.D., Karfunkel, J., Schnellrath, J., & Scholz, R. (2011) Spectroscopic characterization of transition metal impurities in natural montebrasite/amblygonite. *American Mineralogist* **96**, 42–52.

Dudoignon, P., Beaufort, D., & Meunier, A. (1988) Hydrothermal and supergene alterations in the granitic cupola of Montebras, Creuse, France. *Clays and Clay Minerals* **36**(6), 505–520.

Eggins, S.M., Kinsley, M.P.J., & Shelley, J.M.G. (1998) Deposition and element fractionation processes during atmospheric pressure laser sampling for analysis by ICP-MS. *Applied Surface Science* **127–129**, 278–286.

Fransolet, A.-M. & Tarte, P. (1977) Infrared spectra of analyzed samples of the amblygonite–montebrasite series: A new rapid semi-quantitative determination of fluorine. *American Mineralogist* **62**, 559–564.

Fransolet, A.-M., Fontan, F., & de Parseval, P. (2007) Natromontebrasite, a discredited mineral species. *The Canadian Mineralogist* **45**(2), 391–396.

Galliski, M.A., Černý, P., Márquez-Zavalía, M.F., & Chapman, R. (2012) An association of secondary Al-Li-Be-Ca-Sr phosphates in the San Elías pegmatite, San Luis, Argentina. *The Canadian Mineralogist* **50**, 932–942.

Griffin, W.L., Powell, W., Pearson, N.J., & O'Reilly, S.Y. (2008) *GLITTER: Data Reduction Software for Laser Ablation ICP-MS.* ARC National Key Centre for Geochemical Evolution and Metallogeny of Continents, Macquarie University, Sydney, Australia. Available from <http://www.glitter-gemoc.com>.

Kallio, P. (1978) A new X-ray method for the estimation of fluorine content in montebrasites. *American Mineralogist* **63**, 1249–1251.

Kucharik, M. & Vasiljev, R. (2008) Solubility of $AlPO_4$ and $NaVO_3$ in $NaF-AlF_3$ melts. *Journal of Chemical and Engineering Data* **53**, 1817–1819.

Lacroix, A. (1891) Note préliminaire sur un minéral nouveau de Montebras (Creuse). *Bulletin de la Société française de Minéralogie et de cristallographie* **14**, 187–189 (in French).

Lacroix, A. (1895) *Minéralogie de France et de ses colonies*, vol. 1. Béranger, Paris, France, 721 pg. (in French).

Lacroix, A. (1901) *Minéralogie de France et de ses colonies*, *vol*. 3. Ed. Béranger, Paris, France, 818 pg. (in French).

Lacroix, A. (1910) *M*inéralogie *de France et de ses colonies*, *vol*. 4. Ed. Béranger, Paris, France, 923p. (in French).

Lahti, S.I. (1981) On the granitic pegmatites of Eräjärvi area in Orivesi, Southern Finland. *Geological Survey of Finland* **314**, 82 pg.

Liferovich, R.P., Yakovenchuk, V.N., Pakhomovsky, Y.A., Bogdanova, A.N., & Stümpel, G. (1999) Crandallite, goyazite and gorceixite from the Kovdor massif, Russia. *Neues Jahrbüch für Mineralogie Monatshefte* **4**, 145–166.

Liu, Q.-J., Liu, Z.-T., Feng, L.-P., & Tian, H. (2011) First-principles study of structural, elastic, electronic and optical properties of orthorhombic $NaAlF_4$. *Computational Materials Science* **50**, 2822–2827.

Lyalina, L., Selivanova, E., & Hatert, F. (2023) Nomenclature of the triphylite group of minerals. *European Journal of Mineralogy* **35**, 427–437.

Mallard, E. (1859) Géologie de la Creuse. Journal de voyage d'E Mallard (1857–1860). *Mémoire de la Société des Sciences Naturelles et Archéologiques de Creuse* **22**, 141 pg.

Marcoux, E., Barré, B., Pichavant, M., & Poujol, M. (2021) Age et genèse de la coupole granitique a métaux rares (Sn, Li, Nb-Ta, W) de Montebras (Creuse, Massif central français). *Earth Sciences Bulletin* **192**(16), 1–33 (in French).

Mason, B. (1941) Minerals of the Varuträsk pegmatite. XXIII. Some iron-manganese phosphate minerals and their alteration products, with special reference to material from Varutriisk. *Geologiska Föreningens i Stockholm Förhandlingar* **63**, 117–165.

Melleton, J., Gloaguen, E., & Frei, D. (2015) Rare-elements (Li-Be-Ta-Sn-Nb) magmatism in the European Variscan Belt, a review. Proceedings of the 13th SGA Biennial Meeting 2015, August 24th–27th, 2015, Nancy, France (807–810).

Milton, C., Axelrod, J.M., Carron, M.K., & Stearns MacNeil, F. (1958) Gorceixte from Dale County, Alabama. *American Mineralogist* **43**, 688–694.

Moissenet, M.L. (1871) Mémoire sur une nouvelle espèce minérale rencontrée dans le gîte d'étain de Montebras (Creuse). *Annales des Mines* **20**(4), 1–21 (in French).

Moore, P.B. (1982) Pegmatite minerals of P(V) and B(III). *In* Granitic pegmatites in Science and Industry (P. Černý. ed.). *Mineralogical Association of Canada, Short Course Handbook* **8**, 267–291.

Moss, A.A., Fejer, E.E., & Embrey, P.G. (1969) On the X-ray identification of amblygonite and montebrasite. *Mineralogical Magazine* **37**(287), 414–422.

Nagaraja, R., Pushpa Manjari, V., Sailaja, B., & Ravikumar, R.V.S.S.N. (2017) A novel orange emitting Sm^{3+} ions doped $NaCaAlPO_4F_3$ phosphor: Optical and luminescence properties. *Journal of Molecular Structure* **1130**, 96–102.

Nicolas, J. & de Rosen, A. (1963) Phosphates hydrothermaux de basse température et kaolinisation: La gorceixite du massif des Colettes (Allier) et les minéraux associés (hinsdalite). *Bulletin de la Société française de Minéralogie et de Cristallographie* **86**, 379–385 (in French).

Patureau, J., Chiappero, P.J., & Lebocey, J. (2011) Mines et minéraux de Montebras, Soumans (Creuse). *Le Règne Minéral* **99**, 5–34 (in French).

Petrík, I., Kubis, M., Konecny, P., Broska, I., & Malachovsky, P. (2011) Rare phosphates from the Surovec Topaz – Li-Mica Microgranite, Gemeric Unit, Western Carpathians, Slovak Republic: Role of F/H_2O of the melt. *The Canadian Mineralogist* **49**, 521–540.

Prado Araujo, F., Hulsbosch, N., & Muchez, P. (2020) High spatial resolution Raman mapping of complex mineral assemblages: Application on phosphate mineral sequences in pegmatites. *Journal of Raman Spectroscopy* **52**, 690–708.

Prado Araujo, F., Muchez, P., & Hulsbosch, N. (2023a) The magmatic–hydrothermal transition in P-rich pegmatitic melts: Crystal–melt–fluid interactions recorded by phosphate minerals. *Geochimica et Cosmochimica Acta* **356**, 129–148.

Prado Araujo, F., Hulsbosch, N., & Muchez, P. (2023b) Paragenesis and precipitation stages of Nb-Ta-oxide minerals in phosphorus-rich rare-element pegmatites (Buranga dike, Rwanda). *American Mineralogist* **108**, 277–296.

Pushpa Manjari, V., Rama Krishna, Ch., Venkata Reddy, Ch., & Ravikumar, R.V.S.S.N. (2014) Synthesis and spectral investigations of Cu(II) ion-doped $NaCaAlPO_4F_3$ phosphor. *Luminescence* **29**, 1123–1129.

Ramik, R.A., Sturman, B.D., Roberts, A.C., & Dunn, P.J. (1983) Viitaniemiite from the Francon Quarry, Montreal, Quebec. *The Canadian Mineralogist* **21**, 499–502.

Rao, C., Wang, R., Hatert, F., & Baijot, M. (2014) Hydrothermal transformations of triphylite from the Nanping No. 31 pegmatite dyke, Southeastern China. *European Journal of Mineralogy* **26**, 179–188.

Roda-Robles, E., Pesquera, A., De Madinabeitia, S.G., Gil Ibarguchi, J.I., Nizamoff, J., Simmons, W., Falster, A., & Galliski, M.A. (2014) On the geochemical character of primary Fe-Mn-phosphates belonging to the triphylite–lithiophilite, graftonite–beusite, and triplite–zwieselite series: First results and implications for pegmatite petrogenesis. *The Canadian Mineralogist* **52**, 321–335.

Roda-Robles, E., Pesquera, A., Simmons, W., Gil-Crespo, P.P., Webber, K., Nizamoff, J., & Falster, A. (2020) Paragenetic relationships, geochemistry and petrogenetic significance of primary FeMn phosphates from pegmatites: The case study of Cañada (Salamanca, Spain) and Palermo (New Hampshire, USA) pegmatites. *Lithos* **374–375**, 105710.

Roda-Robles, E., Gil-Crespo, P.P., Pesquera, A., Lima, A., Garate-Olave, I., Merino-Martínez, E., Cardoso-Fernandes, J., & Errandonea-Martin, J. (2022) Compositional variations in apatite and petrogenetic significance: Examples from peraluminous granites and related pegmatites and hydrothermal veins from the Central Iberian Zone (Spain and Portugal). *Minerals* **12**, 1401.

Roda-Robles, E., Pesquera, A., Gil-Crespo, P.P., Simmons, W., Webber, K., Falster, A., Errandonea-Martin, J., & Garate-Olave, I. (2024) Apatite as an archive of pegmatite-forming processes: An example from the Berry-Havey pegmatite (Maine, U.S.A.). *American Mineralogist* **109**, 1608–1625.

Shirose, Y. & Uehara, S. (2014) Secondary phosphates in montebrasite and amblygonite from Nagatare, Fukuoka Prefecture, Japan. *Journal of Mineralogical and Petrological Sciences* **109**, 103–108.

Spandler, C., Pettke, T., & Rubatto, D. (2011) Internal and external fluid sources for eclogite-facies veins in the Monviso meta-ophiolite, Western Alps: Implications for fluid flow in subduction zones. *Journal of Petrology* **52**(6), 1207–1236.

Stevko, M., Uher, P., Sejkora, J., Malikova, R., Skoda, R., & Vaculovic, T. (2015) Phosphate minerals from the hydrothermal quartz veins in specialized S-type granites, Gemerska Poloma (Western Carpathians, Slovakia). *Journal of Geosciences* **60**, 237–249.

Tarassoff, P., Horváth, L., & Pfenninger-Horváth, E. (2006) Famous mineral localities: The Francon Quarry, Montreal, Quebec. *The Mineralogical Record* **37**, 5–60.

Taylor, M., Smith, R.W., & Ahler, B.A. (1984) Gorceixite in topaz greisen assemblages, Silvermine area, Missouri. *American Mineralogist* **69**, 984–986.

Thisted, E.W., Haarberg, G.M., & Thonstad, J. (2006) Solubility of $AlPO_4$ in cryolite melts. *Thermochimica Acta* **447**, 41–44.

Vignola, P. (2018) New evidence of alteration of graftonite-(Mn) from the Malpensata pegmatite, Colico municipality, Lecco province, Italy. *The Canadian Mineralogist* **56**, 654–656.

Vignola, P., Diella, V., Ferrari, E.S., & Fransolet, A.M. (2011) Complex mechanisms of alteration in a graftonite + sarcopside + triphylite association from the Luna pegmatite, Piona, Lecco Province, Italy. *The Canadian Mineralogist* **49**, 765–776.

White, J.S. (1981) Barian goyazite from Brazil. *The Mineralogical Record* **12**, 379.

Zaitseva, J.N., Yakimov, I.S., & Kirik, S.D. (2009) Thermal transformation of quaternary compounds in $NaF–CaF_2–AlF_3$ system. *Journal of Solid State Chemistry* **182**, 2246–2251.

Received January 1, 2025. Revised manuscript accepted July 14, 2025.

This manuscript was handled by Guest Editor Jon Errandonea and Editor Stephen Prevec.